Scale-Similarity Subgrid-Scale Turbulence Closure for Supercell Simulations at Kilometer-Scale Resolutions: Comparison Against a Large Eddy Simulation

Shiwei Sun, Bowen Zhou
Key Laboratory for Mesoscale Severe Weather/MOE, School of Atmospheric Sciences, Nanjing University, Nanjing, China

Ming Xue
Center for Analysis and Prediction of Storms, University of Oklahoma, Norman, OK, USA

Kefeng Zhu
Nanjing Joint Institute for Atmospheric Sciences, Chinese Academy of Meteorological Sciences, Nanjing, China

Submitted to Journal of Atmospheric Sciences

**Corresponding author address*:
Ming Xue, CAPS, University of Oklahoma, Norman, OK, USA
E-mail: mxue@ou.edu

ABSTRACT

In numerical simulations of deep convection at kilometer-scale horizontal resolutions, in-cloud subgrid-scale (SGS) turbulence plays an important role in the transport of heat, moisture and other scalars. By coarse-graining a 50 m high-resolution large-eddy simulation (LES) of an idealized supercell storm to kilometer-scale grid spacings ranging from 250 m to 4 km, the SGS fluxes of heat, moisture, cloud and precipitating water contents are diagnosed *a priori*. The kilometer-scale simulations are shown to be within the “gray zone” as in-cloud SGS turbulent fluxes are comparable in magnitude to the resolved fluxes at 4 km spacing, and do not become negligible until ~500 m spacing. Vertical and horizontal SGS fluxes are of comparable magnitudes, both exhibit non-local characteristics associated with deep convection as opposed to local gradient-diffusion type of turbulent mixing. As such, they are poorly parameterized by eddy-diffusivity-based closures. To improve the SGS representation of turbulent fluxes in deep convective storms, a scale-similarity LES closure is adapted to kilometer-scale simulations. The model exhibits good correlations with LES-diagnosed SGS fluxes, and is capable of representing counter-gradient fluxes. In *a posteriori* tests, supercell storms simulated with the refined similarity closure model at kilometer-scale resolutions show better agreement with the LES benchmark in terms of SGS fluxes than those with a turbulent-kinetic-energy-based gradient-diffusion scheme. However, it underestimates the strength of updraft, which is suggested to be a consequence of the model effective resolution being lower than the native grid resolution.

1. Introduction

Operational numerical weather prediction (NWP) models are gradually approaching kilometer-scale horizontal resolutions (see Table 13-7 in Benjamin et al. 2019), whereby the bulk features of deep convective clouds are becoming explicitly resolved (Weisman et al. 1997, Moeng et al. 2010). Naturally, as the resolution increases, subgrid-scale (SGS) contributions to mass and momentum fluxes from the formerly parameterized deep moist convection by cumulus schemes should be gradually tuned down. However, most conventional cumulus schemes designed for mesoscale resolutions are independent of horizontal grid spacing. In practice, at resolutions finer than ~4 km, cumulus schemes in NWP models are often switched off entirely, or only shallow cumulus schemes are retained (Chow et al. 2019). Such models are referred to as convection-permitting/allowing models (CPMs, Schwartz et al. 2009; Clark et al. 2009; Prein et al. 2015) or cloud-resolving models (CRMs, Moeng et al. 2010), and are found to generally perform better without cumulus scheme (Chow et al. 2019). For example, Lean et al. (2008) demonstrated the ability of CPMs to generate more realistic-looking precipitation fields and to improve high precipitation forecasts. Much earlier efforts with a CPM include Xue et al. (2003), Clark et al. (2009) and Pearson et al. (2010) found that at 4 km grid spacing, models can produce realistic diurnal cycles of convective systems. Zhu et al. (2018) evaluated 4 km real-time forecasts over China and found improved prediction of precipitation in terms of spatial distribution, intensity, and diurnal variation than coarser-resolution models.

In the absence of cumulus schemes, SGS turbulence parameterization schemes become solely responsible for parameterizing unresolved fluxes in CPMs. Most models employ such parameterization in the form of planetary boundary layer (PBL) schemes, and conventional PBL schemes are not designed to represent turbulence fluxes in deep moist convection above the boundary layer. Although the parameterization of boundary layer turbulence may be sophisticated, most PBL schemes adopt simple gradient-diffusion representation of fluxes for the free atmosphere. As with cumulus schemes, most PBL schemes do not account for differences in the grid spacing used either and the parameterized fluxes are formulated in the vertical dimension only.

Despite the practical success of CPMs, many studies have revealed the partially-resolved and partially subgrid-scale nature of turbulent fluxes associated with deep moist convection at kilometer resolutions (Bryan and Fritsch 2002; Moeng et al. 2009, 2010; Bryan and Morrison 2011; Lebo and Morrison 2015; Tang and Kirshbaum 2020). Within this range, SGS fluxes are significant and their contribution to the total flow is comparable to that of resolved fields. As a result, kilometer-scale moist convection simulations exhibit both grid-dependency and sensitivity to SGS turbulence parameterization (see Chow et al. 2019 and references therein). A general model challenge for grid spacings comparable to the characteristic length scale of turbulence therefore exists in the *terra incognita* or gray zone of turbulence (Wyngaard 2004). In the gray zone, one key requirement of a SGS turbulence model is scale-adaptivity, which means that the turbulence scheme should be able to modulate its contribution based on the grid spacing. What is more, the SGS turbulent mixings are usually anisotropic at gray zone resolutions because of the large horizontal to vertical grid aspect ratio, so that three dimensional (3D) representation of SGS turbulence is also important (Sullivan et al. 2003; Wyngaard 2004).

One approach to SGS turbulence modeling at kilometer-scale resolutions is to adapt closures originally developed for large-eddy simulations (LESs). LES explicitly resolves large energy-containing eddies while the effect of smaller unresolved eddies on resolved flows is parameterized by a turbulence closure. LES closure is conceptually based on the definition of a spatial filter, which is most often tied to the grid spacing, and is therefore intrinsically scale adaptive. In addition, unlike PBL schemes, LES closures (e.g., Smagorinsky 1963, hereafter Smagorinsky closure; Deardorff 1972, a closure based on the prognostic equation of turbulence kinetic energy (TKE), hereafter 1.5-order TKE closure) provide 3D representation of SGS turbulent fluxes. The innate scale adaptivity and 3D formulation suggest LES closures as potential candidates for gray zone applications. They have been extended to kilometer-scale simulations of both dry convective boundary layer (CBL) (Efstathiou and Beare 2015; Efstathiou et al. 2016; Kurowski and Teixeira 2018) and moist convection (Klemp and Wilhelmson 1978a; Takemi and Rotunno 2003; Fiori et al. 2010; Verrelle et al. 2015, 2017; Shi et al. 2018b,a, 2019; Hanley et al. 2019; Strauss et al. 2019).

The commonly used 1.5-order TKE LES closure was first applied to moist convection by Klemp and Wilhelmson (1978). They adopted the TKE closure developed by Deardorff (1972) for boundary layer LES to storm simulations at a grid spacing of O(1 km), and investigated convective storm dynamics. It is then implemented in community cloud and mesoscale NWP models like CM1 (Bryan and Fritsch 2002), ARPS (Xue et al. 2001) and WRF (Skamarock and Klemp 2008) for severe storm simulations. Takemi and Rotunno (2003) examined the 1.5-order TKE and the Smagorinsky (Smagorinsky 1963) closures for the simulation of idealized squall lines at O(1 km) horizontal grid spacings and found improved simulation results by adjusting constants in the closure schemes. Fiori et al. (2010) compared the performance of a 1D PBL scheme and a 3D TKE-based LES closure applied to a supercell simulation at grid spacings ranging from 200 m to 1 km, and obtained acceptable representation of storm structure, evolution and precipitation with the latter. They noted that simulations with LES closure exhibited convergence with increased resolution while those with PBL scheme did not. Verrelle et al. (2015) further demonstrated that improvements by using an LES closure instead of a PBL scheme in a supercell simulation becomes perceptible at 2 km grid spacing.

The above-mentioned studies mostly focused on the resolved storm structures and precipitation while few have investigated the characteristics of SGS turbulent fluxes associated with deep convection or the behaviors of LES turbulence closures for such applications. By filtering LES of a tropical deep convective system to kilometer grids, Moeng et al. (2010) examined the relationship of the subfilter-scale fluxes and filter-scale variables, and in turn proposed the nonlinear model following Clark et al. (1979) as an alternative turbulence closure (more details are given in section 2b). Later, Moeng (2014) re-derived the same closure based on an updraft-downdraft model framework, and showed *a priori* that the nonlinear closure better represents the forward and backward energy transfer between resolved and SGS components. In an *a priori* analysis of a tropical deep convection LES, Verrelle et al. (2017) found significant SGS counter-gradient thermal fluxes in the convective updraft at kilometer scale, which were attributed to nonlocal moist convection eddy fluxes. Strauss et al. (2019) extended Verrelle's analysis to include the entire cloud life cycle, and found superior representation of heat, moisture, and momentum fluxes by Moeng’s nonlinear model compared to the widely-used Smagorinsky and 1.5-order TKE-based LES closures. Shi et al. (2019) applied the dynamic reconstruction model of Chow et al. (2005) to improve the representation of kilometer-scale SGS fluxes for moist convection. They suggested the ability to account for counter-gradient SGS fluxes as one of the key elements of an appropriate LES closure for gray zone simulations of moist convection.

This study extends the work of Moeng et al. (2010; 2014), Verrelle et al. (2017) and Strauss et al. (2019) to a supercell storm typical of the mid-latitude environment. Based on a 50 m LES of the supercell storm, *a priori* analysis of a scale-similarity-based nonlinear closure and a gradient-diffusion-based 1.5-order TKE closure at kilometer-scale resolutions is conducted. By coarse-graining the benchmark LES, scale-dependent model coefficient for the scale-similarity closure is obtained for a range of grid spacings between 250 m and 4 km. The nonlinear closure is then implemented into a community atmospheric model and evaluated *a posteriori*.

2. Case description and numerical methods

a. Benchmark simulation

LES of a tornadic supercell by Roberts et al. (2016) is used as the benchmark simulation in this study. The storm environment is defined by a sounding derived from a real-data simulation of the 3 May 1999 tornado outbreak in Oklahoma, US (Dawson et al. 2010). The sounding is characterized by a strong convective available potential energy of 4154 J kg^{-1} and a 0-1 km storm-relative helicity of 435 m^2 s^{-2}. More information on how environmental conditions as defined by an atmospheric sounding affect storm type and severity can be found in Thompson and Edwards (2000).

The LES is conducted with the community Advanced Regional Prediction System (ARPS) model (Xue et al., 2000; 2001), on a 64 km × 96 km × 16 km domain with 50 m horizontal and 200 m average vertical resolution. Vertical grid spacing is 20 m near the ground and is stretched progressively to nearly 400 m at the domain top. Open boundary conditions are used on the lateral boundaries. Surface friction is included with a constant drag coefficient of 0.01 while surface sensible and latent heat fluxes are set to zero. The 1.5-order TKE closure of Moeng (1984) based on Deardorff (1972) is used for SGS turbulence, and the Lin scheme for cloud microphysics (Lin et al., 1983). As described in Roberts et al. (2016), the final sounding profiles used to define the storm environment underwent a long period of effectively one-dimensional spinup simulation to reach a steady state with a three-force (Coriolis, pressure gradient and frictional forces) balance so that the environment unaffected by the storm will remain more or less unchanged during the storm simulation. Here the frictional force results from vertical turbulence moment flux divergence while at the surface the moment flux is related to surface drag. As shown in Roberts et al. (2016), the spun-up sounding has a well-mixed boundary layer reaching the 900 hPa level. Not including surface heat or moisture flux within the simulation allows us to focus on the development and evolution of storms as well as associated turbulence activities within the given environment with a fully mixed boundary layer.

The storm is initiated by inserting a 10 km-wide and 1.5 km-deep thermal bubble with a 6 K maximum temperature excess in the center of the domain. In the LES simulation, deep convection develops quickly in the first 600 s, and updraft reaches full intensity by about 900 s. Over the next 25 minutes the supercell storm goes through a splitting cycle, with the right mover being stronger and becoming tornadic (Roberts et al. 2016). In this study, we focus mostly on data between 25 and 40 minutes of simulation when the simulated storm is in the mature stage. More details on the experimental design and model configuration can be found in Roberts et al. (2016).

b. Turbulence closures

As mentioned earlier, two SGS turbulence models are evaluated within kilometer-scale simulations. They represent two typical classes of LES closure, based on the eddy-viscosity and scale-similarity closures, respectively. The 1.5-order TKE closure of Deardorff (1972), which was slightly modified by Moeng (1984), is a widely used eddy-viscosity closure that parameterizes SGS fluxes of momentum and scalar quantities based on the local gradients of resolved flow,

$$\begin{aligned} \overline{u_i u_j} - \bar{u}_i \bar{u}_j &= -K_M \left(\frac{\partial \bar{u}_i}{\partial x_j} + \frac{\partial \bar{u}_j}{\partial x_i}\right), \\ \overline{u_i c} - \bar{u}_i \bar{c} &= -K_H \frac{\partial \bar{c}}{\partial x_i}. \end{aligned} \tag{1}$$

where the overbar is a spatial filter operator, c represents a generic scalar variable. K_M and K_H (m^2 s^{-1}) are the eddy viscosity and diffusivity respectively, where

$$K_M = C_K \sqrt{e} l, \tag{2}$$

C_K = 0.1 is a model constant, e (m^2 s^{-2}) is the TKE, and l (m) is a turbulence length scale set to $(\Delta x \Delta y \Delta z)^{\frac{1}{3}}$ on near-isotropic grids. For anisotropic grids with large aspect ratios (i.e., $\Delta x, \Delta y \gg \Delta z$), horizontal $l_h = (\Delta x \Delta y)^{\frac{1}{2}}$ and vertical $l_v = \Delta z$ length scales are set differently in ARPS. Under stable stratification, l is further constrained by the buoyancy length scale $0.76\sqrt{e}/N$, where N (s^{-1}) is the Brunt-Väisälä frequency. K_H in Eq. (2) is modeled as $K_H = K_M / Pr_T$, where Pr_T is the turbulent Prandtl number set to $1/(1 + 2l_v/\Delta z)$.

As a gradient-diffusion model, the TKE closure does not allow counter-gradient fluxes that are often associated with nonlocal boundary layer convection and moist convection fluxes (Shi et al. 2018; 2019). As such, the TKE closure is purely dissipative and forbids energy backscatter from small to large scales. While down-gradient diffusion is acceptable in the inertial subrange, it can be problematic at gray zone spacings where counter-gradient fluxes and backscatter of TKE becomes significant (Verrelle et al. 2017; Shi et al. 2019; Simon et al. 2019; Strauss et al. 2019).

The other closure examined in this study is the nonlinear model of Clark et al. (1979). The SGS turbulent fluxes are parameterized by horizontal gradients of resolved variables

$$\overline{u_i c} - \bar{u}_i \bar{c} = C_s \frac{\Delta^2}{12} \left(\frac{\partial \overline{u_i}}{\partial x} \frac{\partial \bar{c}}{\partial x} + \frac{\partial \overline{u_i}}{\partial y} \frac{\partial \bar{c}}{\partial y}\right), \tag{3}$$

where Δ is the grid spacing, and C_s=1 is a model constant assuming a Gaussian filter (see Appendix A of Chow 2004). The overbar represents 2D horizontal filtering, which is more appropriate for anisotropic grids at kilometer-scale resolutions[1]. Eq. (3) belongs to a general class of scale-similarity models known as the series expansion models (Stolz et al. 2001). It can be derived by an "un-filtering" or deconvolution procedure applied to the left-hand side of Eq. (3) (Chow 2004). Moeng et al. (2014) interpreted Eq. (3) based on the updraft-downdraft model framework by assuming that horizontal fluctuations of the smallest resolved motions and the largest SGS motions are strongly communicated (i.e., scale-similarity). Based on the algebraic closure of Wyngaard (2004), Hanley et al. (2019) related Eq. (3) to the tilting of horizontal fluxes into the x_i direction. Because the SGS fluxes are formulated as *horizontal* gradients of the resolved variables, we follow Verrelle et al. (2017) and refer to Eq. (3) as the Hgrad closure. Note the right hand side of Hgrad closure is related to the local gradients of resolved flow, so the closure is sensitive to the "effective resolution" of the resolved fields. For a filtered LES constructed through coarse graining (see later in section 2c), the effective resolution approaches $2\sim4\Delta_f$ (Δ_f is the filter scale length) depending on the filter chosen. For regular simulations of an NWP model (in section 2d), the effective resolution tends to be in the $6\sim8\Delta$ range (Skamarock 2004) instead (Δ is the grid spacing). This can affect the performance of SGS closure schemes that rely on $\sim2\Delta$ grid scale information.

Free of the local gradient-diffusion assumption, the Hgrad closure is capable of representing counter-gradient fluxes associated with nonlocal convective transport, and allows backscatter of TKE from SGS to resolved scales (Shi et al. 2019). It has been evaluated in simulations of deep convection in the tropics (Moeng et al. 2010, 2014; Verrelle et al. 2017; Strauss et al. 2019), and yields favorable correlations with the *a priori* obtained SGS fluxes on kilometer-scale grids by filtering benchmark LES data. A mixed model (i.e., a linear combination of Eqs. (1) and (3)) was implemented in the U.K. Met Office Unified Model and evaluated at a horizontal grid spacing of

[1] For a 3D spatial filter, the right-hand side of Eq. (3) should also include the vertical gradients $\frac{\partial \overline{u_i}}{\partial z}\frac{\partial \bar{c}}{\partial z}$.

1.5 km for real cases in England, and found to alleviate overestimation of heavy precipitation (Hanley et al. 2019).

The primary advantage of LES closures for the gray zone is their innate scale adaptivity. The grid spacing Δ is formulated into the closures (e.g., Eqs. (1) and (3)), so that the SGS fluxes decrease as the model resolution is refined. In comparison, conventional 1D PBL schemes adapted to gray zone spacings often require some empirically-determined weighting function $f(\Delta)$ to down-scale the SGS fluxes (Boutle et al. 2014; Shin and Hong 2015; Ito et al. 2015; Zhang et al. 2018). Furthermore, these $f(\Delta)$ functions are largely independent of the local flow, whereas LES closures are flow-dependent and therefore more advantangous as turbulence gets better resolved.

However, inclusion of Δ alone does not guarantee the correct scale-adaptive behavior beyond the inertial subrange where LES closures are originally designed for. When applied to gray zone spacings at kilometer scale, the “universal” constants at LES spacings (i.e., C_k in Eq. (1) and C_s in Eq. (3)) must also be adjusted according to the grid spacing, in order to produce correct SGS fluxes. Balancing explicit resolution of convective cells and SGS dissipation, Takemi and Rotunno (2003) suggested enlarging C_k by a factor of 1.5 to 2 when applying the 1.5-order TKE closure to squall-line simulations at O(1 km) grid spacings. Moeng (2014) and Verrelle et al. (2017) adopted the Hgrad model and recommended values of 5 and 7 for C_s based on *a priori* evaluations of simulated tropical deep convection. Strauss et al. (2019) determined C_s at three different horizontal resolutions (500 m, 1 km, and 2 km), and showed increasing C_s with Δ. These studies all suggest that when applied to gray zone simulations of moist convection, the SGS fluxes increase with grid spacing faster than their explicit Δ dependence, such that the scheme constants should also increase. However, the grid dependence of scheme constants (i.e., $C_s(\Delta)$) has not been fully investigated, especially for severe storm simulations, and will be examined in section 3.

In addition to the built-in scale-adaptivity, another advantage of adapting an LES closure rather than a PBL scheme to the gray zone lies in its 3D formulation of SGS fluxes. Conventional PBL schemes only predict the vertical turbulent fluxes while the horizontal fluxes are ignored based on the underlying SGS horizontal homogeneity assumption. Based on field observations, Wyngaard (2004) showed that when approaching the gray zone, SGS horizontal fluxes become significant and are key to improving model performance in the *terra incognita*. Compared to their vertical counterparts, the horizontal SGS turbulent fluxes at gray zone spacings received less attention in previous investigations, and will be examined in sections 3 and 4.

Last but not least, standard LES closures do not differentiate between the boundary layer and the free troposphere, and parameterize turbulence irrespective of its origin. This provides opportunity for a unified treament of SGS turbulence at gray zone resolutions and beyond. Current scale-adaptive turbulence closure schemes are usually limited to the PBL. In the free troposphere, they usually revert back to 1D non-scale-adaptive local-gradient-diffusion-based formulations. This study focuses on the SGS turbulence parameterization for deep moist convection, not for PBL, however.

c. Coarse-graining benchmark LES

To obtain benchmark solutions at different horizontal resolutions, the LES data introduced in section 2a is coarse-grained (or upscaled) to a range of grid spacings from 250 m to 4 km (i.e., 250 m, 500 m, 1 km, 2 km, and 4 km). Following Verrelle et al. (2017), a horizontal box filter is adopted

$$\overline{\phi}^{\Delta} = \frac{1}{R_x R_y} \sum_i \sum_j \phi_{ij}. \tag{4}$$

Here ϕ represents a generic variable, the overbar with attached Δ represents the horizontal averaging operator, summed over a $R_x \times R_y$ stencil centered at grid point (i, j) on the LES grid. The benchmark SGS flux on a grid of $\Delta_{x,y}$ is therefore

$$\overline{u_i c}^{\Delta} - \overline{u_i}^{\Delta}\bar{c}^{\Delta} = \overline{(u_i - \overline{u_i}^{\Delta})(c - \bar{c}^{\Delta})}^{\Delta} = \overline{u_i'' c''}^{\Delta}, \quad (5)$$

where double primes represent SGS perturbations with respect to the coarse grid. Note that the SGS fluxes on the original LES grid is ignored on the righthand-side of Eq. (5) because of their relatively small magnitudes. When the filter width reaches its domain size limit (L_x, L_y), the SGS flux $\overline{u_i'' c''}^{L}$ in this case represents the total resolved flux. The modeled fluxes are diagnosed by substituting the filtered variable $\overline{\phi}^{\Delta}$ from Eq. (4) into Eqs. (1) and (3).

d. A posteriori simulation setup

A posteriori simulations adopt the same model setup as the benchmark LES described in section 2a, except that the horizontal extent of the numerical domain is increased to 128 km × 128 km in order to reduce the influence of the lateral boundaries. Small 4th-order computational mixing coefficients are adopted (1.0×10^{-3} s^{-1} for the 250 m run and 5.0×10^{-4} s^{-1} for other runs) to minimize the effects of computational mixing compared to turbulent mixing. To avoid large potentially differences in the initial development of storm triggered by the somewhat artificial thermal bubble (e.g., the convective storm is found to be difficult to trigger on the 4 km grid with the same initial bubble) so that we can focus on the evolution of storms in their mature stage in different simulations and the LES benchmark, a "warm start" approach is adopted. The simulations are initialized from filtered LES fields at their respective resolutions at 900 s when the initial storm cell has developed from the initial thermal bubble. 3D fields of the simulations up to 2400 s are then output every 60 s for diagnostic analyses.

Two sets of simulations are performed, with the TKE and Hgrad closures introduced in section 2b, respectively. For the Hgrad closure, scale-dependent model constant $C_s(\Delta)$ is adopted (section 3). The Hgrad closure is implemented for all horizontal and vertical SGS fluxes except for momentum, because attempts to implement the closure to momentum led to decreases in numerical stability. A mixed formulation combing both eddy-diffusivity and scale-similarity closures may lead to improved numerical stability while still retaining the counter-gradient capability of the Hgrad model (Vreman et al. 1996), but is left for future work. Simulations with the TKE closure adopt the default C_k values for all resolutions. This is because, as shown in section 3, the fundamental inconsistency of the gradient-diffusion assumption and the counter-gradient mixing associated with moist convection make it fruitless to optimize C_k at kilometer-scale resolutions on purpose of producing truly SGS fluxes.

3. *A priori* analysis

A priori analysis is conducted based on LES of the supercell to examine the partition of fluxes between resolved and subgrid-scale within the kilometer-scale resolution range from 250 m to 4 km. The magnitudes of the fluxes in vertical and horizontal directions are also compared. The performance of the TKE and Hgrad closures are evaluated and compared across the gray zone resolution range. Scale-dependency of the closure constant in the Hgrad model is further determined.

a. General features of SGS fluxes

Mean profiles of potential temperature θ, water vapor mixing ratio q_v, nonprecipitating water content q_{np} (combined cloud water and ice mixing ratios), and precipitating water content q_p (the sum of rain, snow, and hail mixing ratios) as well their respective vertical SGS fluxes at different horizontal resolutions are presented in the first row of Fig. 1 for 1800 s of simulation, a time when the simulated supercell storm is at its mature stage. The SGS fluxes are diagnosed based on Eq. (5), and then horizontally-averaged as denoted by the angle brackets. Resolved vertical fluxes from the LES are also plotted as references of the total fluxes associated with the storm (labeled as "Resolved" in Fig. 1). A snapshot of the LES at 1800 s during the mature stage of the storm is selected for the analysis, while other times show qualitatively similar results. A function $f(c, x_i) = \overline{u_i''c''}^{\Delta} \cdot (\frac{\partial \overline{c}^{\Delta}}{\partial x_i})$ is defined to distinguish between downgradient (negative) and counter-gradient (positive) SGS fluxes for variable c following Verrelle et al. (2017). The heights where $\langle f(c, x_i) \rangle > 0$ for Δ = 1 km are shaded to indicate the presence of counter-gradient transport in Figs. 1a-d. Overall, the vertical SGS fluxes of θ, q_v, q_{np}, and q_p are all positive across the 250 m to 4 km range except for the cloud top entrainment flux of θ in Fig. 1a, and the downward flux of q_p under the cloud base in Fig. 1d. These reflect upward SGS turbulent transport of heat, moisture, cloud content and precipitating hydrometeors associated with the convective storm. The magnitudes of the SGS fluxes decrease as horizontal resolution is refined for all four state variables as expected.

The mean θ in Fig. 1a is characterized by a stably stratified profile with an increased stratification strength into the stratosphere. Positive $\langle f(\theta, z) \rangle$ is found between 1 to 9 km, indicating counter-gradient turbulent transport of heat at these heights. Heat fluxes reach a global maximum in-between 6 to 8 km above ground level (AGL), where the convective updraft is also the strongest (figure no shown). Downgradient entrainment flux dominates close to the cloud top. The diagnosed heat fluxes from 1 to 4 km spacings are of considerable magnitude compared to the total flux, as will be quantified in the bottom row of Fig. 1. $\langle q_v \rangle(z)$ in Fig. 1b decreases monotonically with height, the upward SGS transport of moisture is therefore mostly downgradient, which might be adequately parameterized by a gradient-diffusion scheme. Vertical profiles of $\langle q_{np} \rangle$ and $\langle q_p \rangle$ in Figs. 1c and 1d exhibit maximum around the height of the cloud anvil at 11 – 12 km AGL, a local peak at about 7 km AGL related to the strongest updraft, and a local peak near the freezing level at about 4 km AGL (this peak is weak for $\langle q_p \rangle$). Counter-gradient transport is observed between 6 to 7, and 9 to 10 km for $\langle \overline{w'' q_{np}''}^{\Delta} \rangle$ and $\langle \overline{w'' q_p''}^{\Delta} \rangle$, and is also found below 4 km AGL for $\langle \overline{w'' q_{np}''}^{\Delta} \rangle$.

The ratios of the SGS to the total flux $R(\Delta) = \langle \overline{w'' c''}^{\Delta} \rangle \,/\, \langle \overline{w'' c''}^{\mathrm{L}} \rangle$ for different fluxes and resolutions are presented in the bottom row of Fig. 1. Large fluctuations in the ratios, for examples those below 1 km in Fig. 1e, are mainly caused by vanishingly small total fluxes (see corresponding region in Fig. 1a). The 4 km grid has comparable resolved and SGS contributions to the vertical fluxes for all four variables. As the resolution is refined, $R(\Delta)$ decreases accordingly. On 2 and 1 km grids, the SGS fluxes contribute to roughly 40% and 20% of the total fluxes of θ and q_{np} at the convective storm levels, and slightly smaller amounts for q_v and q_p. If 10% or less SGS flux contribution is taken as a threshold to define well-resolvedness, Fig. 1 then suggests 500 m as the lower bound of the gray zone for the supercell storm. However, note that the ratios computed here are from *a priori* estimates. Finite difference-based NWP models have an effective resolution of around 6 ~ 8Δ, as opposed to the 2Δ grid cutoff (Skamarock 2004). This means that for an NWP model operating at 1 km resolution, contribution from the SGS fluxes might be 3 or 4 times larger than indicated by Figs. 1e-h because some of the fluxes resolved by the LES are not resolved by the regularly NWP model. In other words, the gray zone of deep convection can extend to hectometer-spacings in practice. Regardless of the actual lower bound, Figs. 1e-h suggest the importance of proper representation of SGS fluxes at kilometer-scale resolutions.

b. Spatial distribution of SGS fluxes

Horizontal cross sections of the filtered horizontal and vertical SGS heat fluxes and the corresponding $f(\theta, x_i)$ for Δ = 1 km are presented in Fig. 2. Other gray zone resolutions produce qualitatively similar results and are not shown. The horizontal cross section is taken at 8 km AGL where the storm updraft is the strongest at the time. Location of the supercell is indicated by the $q_{np} = 1.0\times10^{-6}$ kg kg^{-1} solid black contour line. The updraft core inside the cloud, as indicated by the dashed 10 m s^{-1} w-contour, is shaped like a dumbbell in this particular snapshot, and will split into north- and south-moving storms at later times. The updraft centers are also the centers for vertical vorticity, with the north one rotating clockwise and south anticlockwise due to the tilting of environmental horizontal vorticity (not shown). The rotation pair enhances a cloud-related rearward (east-to-west) descending flow at this level, responsible for the dumbbell shape of the convective core.

The left column of Fig. 2 reveals significant SGS heat fluxes within the clouds, whose magnitudes are much greater than the horizontal mean values presented in Fig. 1a. Comparing $\overline{u''\theta''}^{\Delta}$, $\overline{v''\theta''}^{\Delta}$, and $\overline{w''\theta''}^{\Delta}$ in Figs. 2a, 2c, and 2e shows that the magnitudes of the horizontal and vertical SGS heat fluxes are on the same order. This is in accordance with the characteristics of gray zone fluxes (Wyngaard, 2004), suggesting that horizontal SGS mixing is no longer negligible at kilometer-scale resolutions and should be parameterized properly. The cloudy region on the southern flank of the supercell is free of significant SGS fluxes, as those are mainly stratiform clouds that have been passively advected away from the main system. The observation of horizontal and vertical SGS fluxes with comparable magnitudes is also made for turbulent fluxes of q_v, q_{np}, and q_p (results not shown).

The most prominent feature of the horizontal SGS heat fluxes in Figs. 2a and 2c is the divergence around the updraft core, indicating horizontal heat transport from the storm into the environment. In Fig. 2a, positive and negative $\overline{u''\theta''}^{\Delta}$ dominate over the east and west side of the updraft core, and likewise for $\overline{v''\theta''}^{\Delta}$ in the north-south direction in Fig. 2c. As most regions of $f(\theta, x)$ and $f(\theta, y)$ in Figs. 2b and 2d are negative, the SGS horizontal turbulent exchange between the storm and environment, commonly referred to as cloud entrainment and detrainment, are mostly downgradient at this particular elevation.

In Fig. 2e, large positive $\overline{w''\theta''}^{\Delta}$ takes up almost the entire updraft core, indicating strong upward transport of heat within the core of the storm. In the adjacent down-shear region to the east of the updraft core is the mild downdraft branch of the storm circulation, which is associated with downward $\overline{w''\theta''}^{\Delta}$ of moderate magnitudes. As shown in Fig. 2f, counter-gradient heat fluxes clearly dominate over the updraft core, consistent with the findings of Verrelle et al. (2017) and Strauss et al. (2019) for tropical deep convection. A patch of downgradient heat fluxes on the southwest of the updraft core is mainly due to the down-shear tilting of the updraft, as will be shown in Fig. 3.

Figure 3 presents vertical cross sections of heat fluxes through the location of the maximum *w* at 8 km AGL as indicated by the solid lines AB and CD in Figs. 2a and 2c ($\overline{w''\theta''}^{\Delta}$ is presented along line AB). Overall, Fig. 3 reinforces the characteristics of gray zone heat fluxes found in Fig. 2 with respect to their magnitudes and spatial distribution. Similar to the findings of Fig. 2, vertical and horizontal SGS heat fluxes are of comparable magnitudes throughout the depth of the supercell. The distribution of SGS heat fluxes also exhibit similar spatial patterns, where the convective updraft is dominated by upward vertical heat fluxes in the center and surrounded mainly by divergent horizontal heat fluxes on the periphery. Contours of the flux-gradient product in Fig. 3f again confirm the counter-gradient nature of $\overline{w''\theta''}^{\Delta}$ within the updraft that extends from the cloud base at about 500 m to about 9 km. A narrow strip of downgradient $\overline{w''\theta''}^{\Delta}$ is found on the up-shear side of the slanted storm. This is because tilting of the storm by shear creates locally unstable regions with warm cloudy air below the cold environmental air.

Large regions with horizontal counter-gradient fluxes are found near the convective core in Figs. 3b and 3d, which is different from Strauss et al. (2019), who only found horizontal counter-gradient regions near the top of convective clouds. It is also against conventional expectations from cloud entrainment and detrainment. Analysis of horizontal flux budgets (Wyngaard 2004, Eqs 19-20) show that the tilting term $-T \cdot \overline{w''\theta''}^{\Delta} \cdot (\frac{\partial \overline{u_i}^{\Delta}}{\partial z})$ (T is a time scale) plays a leading role for the horizontal counter-gradient fluxes. For example, the counter-gradient negative $\overline{v''\theta''}^{\Delta}$ between 10 and 12 km AGL in Fig 3c is related to the positive $\overline{w''\theta''}^{\Delta}$ and positive $\frac{\partial \overline{v}^{\Delta}}{\partial z}$ north of the updraft center. In other words, down-shear tilting of the ascending flow and the upward SGS fluxes in the convective core together generate horizontal counter-gradient fluxes. This is also true for other scalars (q_v, q_{np} and q_p), whose horizontal transport also exhibit systematic counter-gradient character (not shown).

c. Correlation coefficients between filtered and modeled SGS fluxes

With the retrieved SGS fluxes from LES, performance of the TKE and the Hgrad closures are first evaluated through correlation between the filtered and the modeled fluxes (i.e., the left- and right-hand sides of Eqs. (1) and (3), respectively. As mentioned in section 2c, the filtered fluxes are obtained according to Eq.(5) directly, while the modeled fluxes are parameterized by using the filtered variables), and are presented in Fig. 4. Note that the scheme constants (i.e., C_K

in Eq. (2) and C_s in Eq. (3)) do not affect the correlation coefficients r. Profiles of r at each level are time-averaged between 25 to 40 min when the storm is in its mature stage. An appropriate SGS model should at least be able to produce positive correlations.

As shown in Fig. 4a, the filtered and the TKE SGS scheme modeled $\overline{w''\theta''}^{\Delta}$ are negatively correlated at all resolutions between 1 and 10 km AGL, and poorly correlated at other heights. In comparison, the Hgrad modeled $\overline{w''\theta''}^{\Delta}$ correlate well with the filtered fluxes, with *r*(z) ~ 0.5 for the most of the deep cloud layer at 4 km resolution, and gradually increases to about 0.7 at 250 m resolution. Slight decrease of *r*(z) towards the ground surface and cloud top are observed for the Hgrad model, especially on 4 km grid. This is mainly due to a limited number of cloudy grid points and the small magnitude of fluxes at these elevations as shown in Fig. 1.

Unlike heat fluxes, the TKE model is able to achieve positive correlations for $\overline{w''q_v''}^{\Delta}$ throughout the depth of the storm. This is because $\overline{w''q_v''}^{\Delta}$ is directed downgradient of $\overline{q_v}^{\Delta}(z)$ as shown earlier in Fig. 1b. But even so, the correlation coefficients for the Hgrad modeled $\overline{w''q_v''}^{\Delta}$ are still higher for most of the resolutions considered, especially for the levels above 10 km.

For $\overline{w''q_{np}''}^{\Delta}$ and $\overline{w''q_p''}^{\Delta}$ in Figs. 4c and 4d, r(z) of the TKE closure are close to zero for all gray zone resolutions tested, and are negative at some levels near or under the cloud base. For the Hgrad closure, r(z) are positive with values comparable to those of $\overline{w''\theta''}^{\Delta}$ and $\overline{w''q_v''}^{\Delta}$, except for some decreases in $\overline{w''q_p''}^{\Delta}$ for 4 km and 2 km resolutions at about 4 km AGL, roughly the melting level where the gradients of hydrometeors are large. Figures 4a, 4c and 4d point to a fundamental deficiency of the TKE closure that could not possibly be ameliorated through tuning of scheme constants. As we shall further elaborate with Figs 7 and 8, this is due to the TKE closure's inability to represent counter-gradient fluxes of potential temperature and cloud contents.

Correlation profiles for horizontal SGS fluxes of all scalars selected in this work show similar trends, so only those for $\overline{u''\theta''}^{\Delta}$ is presented in Fig. 4e. r(z) for the Hgrad model again exceeds that for the TKE model at almost all elevations, for all resolutions considered. Three components of the Reynolds stresses tensor $\overline{u''w''}^{\Delta}$, $\overline{u''u''}^{\Delta}$, and $\overline{w''w''}^{\Delta}$ are presented in Figs. 4f-4h. Correlation profiles for the other deviatoric flux profiles qualitatively resemble those for $\overline{u''w''}^{\Delta}$ and are not plotted. In Fig. 4f, the TKE modeled $\overline{u''w''}^{\Delta}$ are poorly correlated with filtered flux even at 250 m resolution. The Hgrad model, on the other hand, predicts higher correlations which increase with improved horizontal resolution. For the horizontal and vertical velocity variances $\overline{u''u''}^{\Delta}$ and $\overline{w''w''}^{\Delta}$, the Hgrad model produces consistently high positive correlation across the gray zone resolutions. As will be shown later in Fig. 9, with the scale-aware coefficients, the Hgrad model can give very good prediction of the SGS TKE.

While the Hgrad model exhibits better correlations than the TKE model in general, the r(z) values often degrade below the cloud base especially at 2 and 4 km resolution. Note that the benchmark simulation was driven with zero sensible and latent surface heat fluxes, so boundary layer is close to neutral and there is not much turbulence activity in the boundary layer. Therefore, fidelity of the Hgrad model within the boundary layer cannot be adequately assessed, and should be investigated in a future study.

d. Coefficients C_s in Hgrad closure

The consistent high correlations between the filtered and the Hgrad modeled fluxes in Fig. 4 suggest the Hgrad closure as a suitable SGS model for simulating deep convective storm at kilometer-scale resolutions. We then proceed to determine its scheme constant C_s based on the root-mean-square values of the left- and right-hand sides of Eq. (3). C_s is computed over the vertical range between 1 to 14 km that includes almost the entire depth of the storm. It is then time averaged between 25 to 40 min during the mature stage of the storm. Although the vertical profiles of the spatial- and temporal-averaged C_s exhibit some moderate fluctuations with height (not shown), for simplicity it is further depth-averaged to obtain a single value for a particular resolution. The procedure is repeated for all SGS fluxes and results are presented in Fig. 5. Coefficients for scalar and momentum fluxes are determined separately. The C_s values obtained for scalars are found to exhibit different resolution dependence for the vertical and horizontal fluxes, possibly due to grid anisotropy at gray zone resolutions. Therefore, two coefficients $C_{s,v}$ and $C_{s,h}$ are determined for vertical and horizontal directions, respectively.

In general, the retrieved $C_{s,v}$ and $C_{s,h}$ exhibit monotonic increase with resolution from a value of 2 at 250 m spacing, to about 13 for $C_{s,v}$ and 8 for $C_{s,h}$ at 4 km spacing. Increased data scatter is found at coarser resolutions as indicated by the wider error bars. This is partly due to a lack of samples as the grid spacing gets wider. The SGS fluxes of the four scalars investigated (i.e., θ, q_v, q_{np} and q_p) produce similar and consistent $C_s(\Delta)$ curves. The intra-scalar variations at a given resolution are small compared to the changes of C_s with respect to Δ. As shown in Fig. 5a, $C_{s,v}$ is around 6 at 1 km resolution, which is close to the values of 5 proposed by Moeng (2014) and 7 by Verrelle et al. (2017) and Strauss et al. (2019) for kilometer-resolution simulations of tropical deep convection.

The increase of C_s with Δ in Figs. 5a and 5b confirms that the explicit grid dependence of the Hgrad closure (i.e., Δ^2 on the right-hand side of Eq. (3)) alone is not enough to account for changes of the SGS fluxes at gray zone resolutions. The range of $C_s(\Delta)$ further suggests that it should not be treated as a constant over the kilometer-resolution range. Grid dependent $C_s(\Delta)$ curves averaged over the fluxes presented in Figs. 5a and 5b are empirically fitted by power series

$$\begin{aligned} C_{s,v}(\Delta) &= 0.074\Delta^{0.63}, \\ C_{s,h}(\Delta) &= 0.27\Delta^{0.41}, \end{aligned} \tag{6}$$

where Δ is measured in units of meters. The C_s for momentum (C_m) also show grid-dependency (in Fig. 5c), and the $C_m(\Delta)$ curves for vertical covariances $\overline{u''w''}^{\Delta}$ and $\overline{v''w''}^{\Delta}$ are fitted as

$$C_m(\varDelta) \;=\; 0.11\varDelta^{0.54}. \tag{7}$$

Other components of the stress tensor are not fitted due to their relatively wide spread.

e. Profile and distribution of modeled SGS fluxes

With the scale-dependent coefficients $C_s(\Delta)$, vertical profiles of the Hgrad modeled $\overline{w''\theta''}^{\Delta}$ and $\overline{u''\theta''}^{\Delta}$ are computed and presented alongside the LES filtered fluxes in Fig. 6. Modeled fluxes by the TKE closure with its default constant $C_k = 0.1$ are also plotted for comparison. Dashed lines in Fig. 6 are from the online simulations that will be discussed in the following section. The modeled $\overline{w''\theta''}^{\Delta}$ values from the Hgrad scheme agree reasonably well with their respective filtered-LES fluxes from 250 m to 4 km, although growing discrepancies are found for coarse resolution results. In comparison, profiles of the TKE scheme are completely off with wrong signs.

For the horizontal fluxes $\overline{u''\theta''}^{\Delta}$ in the bottom row of Fig. 6, the Hgrad model is able to reproduce the filtered-LES profiles reasonably well at gray zone resolutions. The TKE model, on the other hand, is able to produce fluxes with the right signs. This is expected based on the correlation profiles in Fig. 4e, which shows the largely downgradient nature of horizontal fluxes on kilometer-scale grids (see also Figs. 2b and 3b). The flux profiles of the TKE model also have similar shapes as that of the LES filtered fluxes, and therefore could be improved by tuning up the model constant C_k as suggested by Takemi and Rotunno (2003). The diagnosed fluxes of other variables (except for $\overline{w''q_v''}^{\Delta}$) show similar patterns to $\overline{u''\theta''}^{\Delta}$, which is consistence with the results of Fig. 4 and are not presented here.

Besides horizontally-averaged profiles, horizontal and vertical cross sections of the modeled heat fluxes are presented in Figs. 7 and 8 to evaluate the ability of LES closures to reproduce the spatial distribution of SGS fluxes. The modeled fluxes are evaluated against the LES filtered fluxes presented earlier in Figs. 2 and 3. For the horizontal fluxes, the TKE and Hgrad closures are both able to reproduce the most prominent feature of divergent fluxes away from the updraft core. However, the TKE fluxes in Figs. 7a and 7c show spurious horizontal wave features down-shear of the updraft, corresponding to the wavy storm outflow shown in Fig. 2. The horizonal distribution of the Hgrad fluxes compare better with that of Figs. 2a and 2c, although it predicted some small fluxes out of the storm over the stratiform region that is absent in the filtered-LES results.

Contours of the modeled $\overline{w''\theta''}^{\Delta}$ show distinct differences between the two closures. The TKE closure fails to produce upward $\overline{w''\theta''}^{\Delta}$ for most part inside the updraft core in Fig. 7e due to its eddy-viscosity formulation. The TKE closure is only capable of capturing the small region of positive $\overline{w''\theta''}^{\Delta}$ on the southwest corner of the updraft core in Fig. 7e, because the fluxes are downgradient as shown in Fig. 2f as a results of the down-shear storm tilt. The Hgrad modeled fluxes in Fig. 7f compare well with LES benchmark in Fig. 2e, especially within the updraft core where vigorous upward heat fluxes occur.

Vertical cross sections of the modeled fluxes in Fig. 8 reinforce the observations made from Fig. 7. The TKE modeled $\overline{u''\theta''}^{\Delta}$ and $\overline{v''\theta''}^{\Delta}$ bear some resemblance to the filtered LES results in Figs. 3a and 3c, although they appear overly-smooth and miss regions where the horizontal counter-gradient transport exist. In comparison, the Hgrad model is able to capture most of the fine-scale fluctuations, and compares quite well with that of Fig. 3. In Fig. 8e, the TKE closure predicts spurious downward pointing $\overline{w''\theta''}^{\Delta}$ over all counter-gradient regions outlined in Fig. 3f. The distribution of the filtered LES fluxes in Fig. 3e is reproduced well by the Hgrad model in Fig. 8f.

The last point we wish to make about the Hgrad model in this section is its ability to represent SGS TKE. Unlike eddy-viscosity models, the trace of the stress tensor predicted by a scale-similarity model can offer useful predictions the SGS TKE (Zhou and Chow 2011). Figure 9 presents the vertical profiles of the horizontal-averaged TKE diagnosed by the Hgrad model along with the filtered LES profiles at gray zone resolutions. Good overall agreement with the filtered LES profiles is achieved by the Hgrad model, except for some discrepancy for the 2 km resolution results in Fig. 9d and some moderate overprediction for the 4 km resolution results in Fig. 9e. Overall, the favorable comparison suggests that Eq. (3) could alternatively be used as a diagnostic tool for SGS TKE in kilometer-scale simulations of deep convection.

4. Results of *a posteriori* simulations

Given favorable *a priori* evaluations, the Hgrad model with scale dependent coefficient $C_s(\Delta)$ is implemented in ARPS for all scalars. Results of the online *a posteriori* simulations described in section 2d are presented here. Except for the 4 km simulations, all other finer-resolution simulations are capable of simulating the supercell storm. On the 4 km grid however, the storm cell present at 900 s undergoes rapid decay and the supercell fails to further develop with either SGS models. For grid spacings of 2 km and finer, the evolution and structure of supercells in Hgrad simulations broadly resemble those of TKE simulations at the same grid spacing although differences do exist in detail, which will be illustrated later.

Horizontally-averaged profiles of the simulated $\overline{w''\theta''}^{\Delta}$ and $\overline{u''\theta''}^{\Delta}$ at 1800 s are presented alongside with their offline diagnosed counterparts in Fig. 6. For vertical fluxes in the first row of Fig. 6, profiles from Hgrad model show good overall agreement with the LES profiles at gray zone resolutions of 250 m, 500 m, and 1 km. At 2 km resolution, a prevalent underprediction of $\overline{w''\theta''}^{\Delta}$ is found below 8 km AGL, which could be improved slightly by tuning up $C_{s,v}$ further than what Eq. (7) dictates. At 4 km resolution, the field is too smooth, so the $\overline{w''\theta''}^{\Delta}$ is vanishingly small.

The TKE model, on the hand, has no predictive capability of the counter-gradient vertical fluxes as expected. In fact, the modeled $\overline{w''\theta''}^{\Delta}$ by the TKE closure vanishes at resolutions beyond 500 m. This is due to the rapid drop of the predicted TKE at coarse gray zone resolutions, hence a diminishing mixing coefficient according to Eq. (2). It is confirmed by plotting the vertical profiles of TKE by the TKE closure in Fig. 9. The severe under-estimation of TKE is a direct result of the SGS closure's inability to represent counter-gradient heat fluxes, and therefore missing the essential buoyancy production source term in the prognostic TKE equation (Verrelle et al. 2017).

In the bottom row of Fig. 6, the simulated horizontal heat fluxes by the Hgrad model also compares well with the LES benchmark from 250 m to 2 km resolutions, except for some over-prediction on the finest 250 m grid. Similar to $\overline{w''\theta''}^{\Delta}$, the TKE predicted $\overline{u''\theta''}^{\Delta}$ is also close to zero at all resolutions due to the underprediction of TKE. Besides θ, vertical flux profiles of other scalars by the Hgrad model also show agreement with their respective LES profiles (results not shown). The derived TKE from the Hgrad simulations have profiles with similar shape to the LES except for 4-km resolution (Fig. 9). At finer grid spacings of 250 m and 500 m, the Hgrad model also overpredicts TKE compared to the LES benchmark. TKE from the TKE closure is under-predicted at 500 m and nearly zero for large grid spacings, and somewhat over-predicted at 250 m.

Aside from the SGS flux profiles, vertical profiles of the horizontally-averaged resolved and total heat fluxes are presented in Fig. 11. Simulated profiles of resolved heat flux are similar for both SGS models at 250 m and 500 m resolutions, and agree well with the filtered LES profiles. At 1 and 2 km resolutions, the TKE model produces stronger resolved upward heat flux (and also stronger updraft) than the Hgrad model, which compensates for its underestimated SGS $\overline{w''\theta''}^{\Delta}$ such that the total upward heat flux profiles turn out to be very similar for the two models. The compensating behavior of the resolved fluxes to the TKE model at gray zone spacings is similar to the previous findings for boundary layer turbulence (Simon et al. 2019). The reason is likely complicated and deserves its own future study. Briefly, one plausible explanation is that as the TKE model transports heat in the wrong direction downwards, the vertical stability is weakened to allow for stronger updraft. It could also be due to the limited horizontal SGS mixing of the TKE model as shown in Fig. 6 and later in Fig. 12 such that the convective updraft stays relatively undiluted. Lastly, at 4 km resolution, the supercell fails to develop so neither model produces any upward heat flux.

Next, horizontal and vertical cross sections of the modeled heat fluxes are examined for 1 km resolution results. Figure 11 presents the contours of the SGS heat fluxes at 8 km AGL for the TKE and Hgrad models. The storm morphology, as outlined by the cloud contour, appears different in the online simulations due to the feedback of the SGS fluxes on the resolved flow. For the TKE closure, the magnitudes of both vertical and horizontal heat fluxes are much smaller than the filtered LES fields presented in Fig. 2 due to underestimation of TKE. The resulting updraft core is also much smaller in Fig. 11a, and has already split into northward and southward moving parts at 8 km AGL. The horizontal (Figs. 11b and 11d) and vertical (Fig. 11f) heat fluxes predicted by the Hgrad closure show similar magnitudes and distribution as the filtered LES results. The flux fields however, appear much smoother than the diagnosed fluxes presented in Fig. 7, likely a result of the coarser effective resolution of the finite-difference model. Compared to the TKE closure, Hgrad closure produces stronger horizontal mixing between the convective updraft and the environmental air, which could decrease the buoyancy of the updraft core. The predicted updraft core is broader than that of the TKE model and remains connected as the LES results, although the overall area of the updraft core is still somewhat smaller. Vertical cross sections in Fig. 12 indicate similar results for the SGS heat fluxes. However, the TKE closure produces stronger updrafts compared to the Hgrad closure, which might be related to the wrong vertical downward and the weaker horizontal outward SGS heat fluxes in the TKE scheme, as mentioned before. Similar behavior was also noted by Hanley et al. (2019). Compared to the results of filtered LES, the updraft produced by Hgrad closure is also weaker, which could be due to coarser effective resolutions.

To illustrate the influence of SGS closures on the storm structure, horizontal and vertical cross sections of the simulated supercells at 1 km resolution as well as the filtered LES field are presented in Fig. 13. The time chosen is 2100 s, 5 minutes after the above analyses, to let the impacts accumulate. By this time, the supercell storm has undergone at least one splitting (Klemp and Wilhelmson 1978b), and the right-moving cell becomes the dominant one and is located close to the center of plotted domain in Fig. 13. The left-moving cell near the northwestern corner of the plotted domain in Fig. 13 are much smaller and weaker, especially in Hgrad (Fig. 13e) and TKE (Fig. 13c) simulations. In the right-moving cell of LES (Fig. 13a), strong mesocyclone rotation near the updraft core within the simulated supercell is clearly seen from the wind vectors at 1 km height level, and also suggested by the hook-shaped reflectivity echo wrapping around the updraft core. These features are also evident in the TKE (Fig. 13c) and Hgrad (Fig. 13e) simulations except that the rotation is weaker and the hook is less pronounced, and more so in Hgrad simulation. The near surface cold pool in all simulations, as outlined by the -0.5 K perturbation potential temperature contours, are similar in size. In the vertical cross section along the low-level inflow and cutting through the low-level updraft core, a weak echo vault is found underneath the most intense reflectivity core between 4 and 5 km (Fig. 13b), which is a structure characteristic of intense supercell storm. Generally similar structures are found in TKE and Hgrad simulations, although the strong echo top is noticeably lower in both simulations than LES (about 6.7 km and 6 km high, respectively, versus ~8 km in LES), as well as the low-level updrafts. The resolution difference should be the main reason for the differences from LES simulation, while the difference between TKE and Hgrad simulations are due to the turbulence parameterization schemes as mentioned before.

Time series of the domain-averaged precipitation rate is presented in Fig. 14. The precipitation rates at the resolutions of 250 m and 500 m are similar for both SGS turbulence closures and are close to that of the LES. For grid spacings of 1 km and 2 km, the first rainfall peak in the TKE simulations is larger than that of the Hgrad scheme, consistent with the stronger simulated updrafts. For resolutions coarser than 1 km, delays in the onset of precipitation are observed. At 2 km resolution, rainfall rates quickly spike beyond the LES benchmark once initiated and fall back shortly after, while the LES show sustained rainfall. In spite of this, the Hgrad closure certainly performs better than the TKE closure, given its longer sustained high rainfall period (25-35 min) and less overpredicted rainfall rate. At 4 km resolution, further delays are found for the onset of rainfall, and both simulated rainfall rates exhibit faster decay. Although the Hgrad model still shows better agreement with the LES benchmark than the TKE closure in terms of the maximum rain rate reached, the rain rate curves essentially suggest that 4 km resolution is most likely too coarse to allow explicit resolution of the supercell, imposing a numerical limit that could not be easily overcome by improving SGS turbulence closure alone. Potvin and Flora (2015) also found that 4-km grid spacing was too coarse to reliably simulate supercells. In real cases, sustained convection can often develop within CPMs at 4 km grid spacing (e.g., Zhu et al. 2018) due to, for example, boundary layer convergence forcing or orographic lifting, which are absent in the current simulations. Applying the proposed scheme to real cases is a goal of our future studies.

Summary and future work

By coarse-graining a high resolution LES of a supercell storm, *a priori* analysis is first conducted to examine the characteristics of SGS turbulence fluxes at typical convection-resolving/allowing resolutions from 250 m to 4 km. It is shown that at kilometer-scale resolutions, the deep convective storm is only partially resolved and partially subgrid scale. Vertical SGS fluxes of heat, moisture, cloud ice/water contents and precipitating hydrometeor contents account for as large as 50% of the total fluxes on a 4 km grid and do not drop below 10% until the grid spacing is refined to 500 m, confirming that kilometer-scale resolutions are in fact in the gray zone for deep convection as previous studies have suggested. Close examination of the SGS fluxes suggests the need for a three-dimensional representation of SGS turbulence, as the horizontal and vertical SGS fluxes are of comparable magnitudes. The in-storm vertical SGS fluxes exhibit prominent counter-gradient features especially within the storm updrafts where counter-gradient fluxes are dominant. Horizontal SGS fluxes are mainly characterized by divergence around the updraft at the upper levels, representing turbulent mixing between the cloud and the environment. They are mostly downgradient at kilometer-scale resolutions, but are counter-gradient in some regions related to the tilting of the updraft core.

The possibility of extending LES turbulence closures to kilometer-scale simulations of deep convection is considered, because LES closures are both grid-dependent and 3D by formulation, which satisfies the key requirements for SGS turbulence model at gray zone resolutions. With the filtered LES data as benchmark, two LES closures (TKE and Hgrad) at kilometer-scale resolutions are evaluated *a priori*. The TKE scheme is a classic eddy-diffusivity scheme based on gradient-diffusion assumptions, while the Hgrad scheme is a scale-similarity model that permits counter-gradient fluxes. Correlations between the filtered LES fluxes and the modeled fluxes by the turbulence closures favor the Hgrad model, which is able to achieve average values between 0.5-0.7 at kilometer-scale resolutions. The TKE closure gives negative correlations for vertical heat fluxes and almost zeros correlation for cloud contents and precipitating hydrometeor contents. Examination of horizontal and vertical distributions of the SGS heat fluxes further shows that Hgrad model is able to reproduce the dominant upward heat fluxes in the storm core, and is better at capturing fine scale variations within the storm than the TKE scheme. Overall, the Hgrad modeled fluxes compare well with the LES benchmark, while TKE model performs poorly due mostly to its inability to represent counter-gradient fluxes.

Given the favorable *a priori* assessment, coefficients of the Hgrad model are computed for different gray zone resolutions for the supercell storm simulation. Considering the anisotropy of the gray zone grids, the coefficients are split into horizontal and vertical directions. Both coefficients increase monotonically with grid spacing in the gray zone range, and are each fitted with a power series. The Hgrad model with such scale (grid spacing) awareness is implemented into community atmospheric model ARPS, and *a posteriori* simulations of the supercell storm on kilometer-scale grids are conducted. Comparison of these online simulations with the LES benchmark show that the Hgrad model is indeed able to give decent representations of both vertical and horizontal SGS fluxes in the resolution range between 250 m to 2 km. The simulated flux fields appear smoother than the LES benchmark due mostly to the effective resolution of the finite-difference model. Storm structures are also well reproduced with the Hgrad model, except for moderate underestimations of the updraft intensity. In contrast, simulations with TKE closure produce erroneous downward SGS heat fluxes in the vertical direction, and weaker SGS mixing between the convective and environmental air in the horizontal direction for most resolutions. At 4 km, both models show systematic underpredictions of vertical fluxes, and also severe underpredictions of rainfall. This suggests that at 4 km grid spacing, neither model is able to overcome the numerical deficiency of low spatial resolution. 4 km is simply too low a resolution to accurately resolve supercell storms, consistent with the earlier study of Potvin and Flora (2015).

Overall, the Hgrad closure presents promising prospects as a more accurate SGS turbulence closure model for kilometer-scale simulations of deep convection. Performance of model will be further evaluated for other types of storms and real cases to determine its suitability for convective scale weather prediction at convection-resolving/allowing resolutions, and to optimize the scale-dependent coefficients. Future work also plans to investigate the interactions between SGS turbulence with microphysics on gray zone grids.

Acknowledgments. We thank Brett Roberts for providing LES data, which was performed at the Texas Advanced Supercomputing Center, an NSF XSEDE facility. This work was supported by the National Key R&D Program of China (Grant 2018YFC1507304). Numerical simulations were performed at the National Supercomputing Center in Tianjin, China.

References

Benjamin, S. G., J. M. Brown, G. Brunet, P. Lynch, K. Saito, and T. W. Schlatter, 2019: 100 Years of Progress in Forecasting and NWP Applications. *Meteor. Monogr.*, **59**, 13.1-13.67, https://doi.org/10.1175/AMSMONOGRAPHS-D-18-0020.1.

Boutle, I. A., J. E. J. Eyre, and A. P. Lock, 2014: Seamless Stratocumulus Simulation across the Turbulent Gray Zone. *Mon. Wea. Rev.*, **142**, 1655–1668, https://doi.org/10.1175/MWR-D-13-00229.1.

Bryan, G. H., and J. M. Fritsch, 2002: A Benchmark Simulation for Moist Nonhydrostatic Numerical Models. *Mon. Wea. Rev.*, **130**, 2917–2928, https://doi.org/10.1175/1520-0493(2002)130<2917:ABSFMN>2.0.CO;2.

——, and H. Morrison, 2011: Sensitivity of a Simulated Squall Line to Horizontal Resolution and Parameterization of Microphysics. *Mon. Wea. Rev.*, **140**, 202–225, https://doi.org/10.1175/MWR-D-11-00046.1.

Chow, F. K., 2004: Subfilter-scale turbulence modeling for large-eddy simulation of the atmospheric boundary layer over complex terrain. Ph.D. thesis, Stanford University.

——, R. L. Street, M. Xue, and J. H. Ferziger, 2005: Explicit filtering and reconstruction turbulence modeling for large-eddy simulation of neutral boundary layer flow. *J. Atmos. Sci.*, **62**, 2058–2077, https://doi.org/10.1175/JAS3456.1.

——, C. Schär, N. Ban, K. A. Lundquist, L. Schlemmer, and X. Shi, 2019: Crossing Multiple Gray Zones in the Transition from Mesoscale to Microscale Simulation over Complex Terrain. *Atmosphere*, **10**, 274, https://doi.org/10.3390/atmos10050274.

Clark, A. J., W. A. Gallus, M. Xue, and F. Kong, 2009: A Comparison of Precipitation Forecast Skill between Small Convection-Allowing and Large Convection-Parameterizing Ensembles. *Wea. Forecasting*, **24**, 1121–1140, https://doi.org/10.1175/2009WAF2222222.1.

Clark, R. A., J. H. Ferziger, and W. C. Reynolds, 1979: Evaluation of subgrid-scale models using an accurately simulated turbulent flow. *J. Fluid Mech.*, **91**, 1–16, https://doi.org/10.1017/S002211207900001X.

Dawson, D. T., M. Xue, J. A. Milbrandt, and M. K. Yau, 2010: Comparison of Evaporation and Cold Pool Development between Single-Moment and Multimoment Bulk Microphysics Schemes in Idealized Simulations of Tornadic Thunderstorms. *Mon. Wea. Rev.*, **138**, 1152–1171, https://doi.org/10.1175/2009MWR2956.1.

Deardorff, J. W., 1972: Numerical Investigation of Neutral and Unstable Planetary Boundary Layers. *J. Atmos. Sci.*, **29**, 91–115, https://doi.org/10.1175/1520-0469(1972)029<0091:NIONAU>2.0.CO;2.

Efstathiou, G. A., and R. J. Beare, 2015: Quantifying and improving sub-grid diffusion in the boundary-layer grey zone. *Q.J.R. Meteorol. Soc.*, **141**, 3006–3017, https://doi.org/10.1002/qj.2585.

——, ——, S. Osborne, and A. P. Lock, 2016: Grey zone simulations of the morning convective boundary layer development. *J. Geophys. Res. Atmos.*, **121**, 2016JD024860, https://doi.org/10.1002/2016JD024860.

Fiori, E., A. Parodi, and F. Siccardi, 2010: Turbulence Closure Parameterization and Grid Spacing Effects in Simulated Supercell Storms. *J. Atmos. Sci.*, **67**, 3870–3890, https://doi.org/10.1175/2010JAS3359.1.

Hanley, K., M. Whitall, A. Stirling, and P. Clark, 2019: Modifications to the representation of subgrid mixing in kilometre- scale versions of the Unified Model. *Quart. J. Roy. Meteor. Soc.*, **145**, 3361–3375, https://doi.org/10.1002/qj.3624.

Ito, J., H. Niino, M. Nakanishi, and C.-H. Moeng, 2015: An Extension of the Mellor-Yamada Model to the Terra Incognita Zone for Dry Convective Mixed Layers in the Free Convection Regime. *Bound.-Layer Meteor.*, **157**, 23–43, https://doi.org/10.1007/s10546-015-0045-5.

Klemp, J. B., and R. B. Wilhelmson, 1978a: The Simulation of Three-Dimensional Convective Storm Dynamics. *J. Atmos. Sci.*, **35**, 1070–1096, https://doi.org/10.1175/1520-0469(1978)035<1070:TSOTDC>2.0.CO;2.

——, and ——, 1978b: Simulations of Right- and Left-Moving Storms Produced Through Storm Splitting. *J. Atmos. Sci.*, **35**, 1097–1110, https://doi.org/10.1175/1520-0469(1978)035<1097:SORALM>2.0.CO;2.

Kurowski, M. J., and J. Teixeira, 2018: A Scale-Adaptive Turbulent Kinetic Energy Closure for the Dry Convective Boundary Layer. *J. Atmos. Sci.*, **75**, 675–690, https://doi.org/10.1175/JAS-D-16-0296.1.

Lean, H. W., P. A. Clark, M. Dixon, N. M. Roberts, A. Fitch, R. Forbes, and C. Halliwell, 2008: Characteristics of High-Resolution Versions of the Met Office Unified Model for Forecasting Convection over the United Kingdom. *Mon. Wea. Rev.*, **136**, 3408–3424, https://doi.org/10.1175/2008MWR2332.1.

Lebo, Z. J., and H. Morrison, 2015: Effects of Horizontal and Vertical Grid Spacing on Mixing in Simulated Squall Lines and Implications for Convective Strength and Structure. *Mon. Wea. Rev.*, **143**, 4355–4375, https://doi.org/10.1175/MWR-D-15-0154.1.

Lin, Y.-L., R. D. Farley, and H. D. Orville, 1983: Bulk parameterization of the snow field in a cloud model. *J. Climate Appl. Meteor.*, **22**, 1065–1092, https://doi.org/10.1175/1520-0450(1983)022<1065:BPOTSF>2.0.CO;2.

Moeng, C.-H., 1984: A Large-Eddy-Simulation Model for the Study of Planetary Boundary-Layer Turbulence. *J. Atmos. Sci.*, **41**, 2052–2062, https://doi.org/10.1175/1520-0469(1984)041<2052:ALESMF>2.0.CO;2.

——, 2014: A Closure for Updraft–Downdraft Representation of Subgrid-Scale Fluxes in Cloud-Resolving Models. *Mon. Wea. Rev.*, **142**, 703–715, https://doi.org/10.1175/MWR-D-13-00166.1.

——, M. A. LeMone, M. F. Khairoutdinov, S. K. Krueger, P. A. Bogenschutz, and D. A. Randall, 2009: The Tropical Marine Boundary Layer Under a Deep Convection System: a Large-Eddy Simulation Study. *Journal of Advances in Modeling Earth Systems*, **1**, https://doi.org/10.3894/JAMES.2009.1.16.

Moeng, C.-H., P. Sullivan, M. Khairoutdinov, and D. Randall, 2010: A mixed scheme for subgrid-scale fluxes in cloud-resolving models. *J. Atmos. Sci.*, **67**, 3692–3705, https://doi.org/10.1175/2010JAS3565.1.

Pearson, K. J., R. J. Hogan, R. P. Allan, G. M. S. Lister, and C. E. Holloway, 2010: Evaluation of the model representation of the evolution of convective systems using satellite observations of outgoing longwave radiation. *J. Geophys. Res.*, **115**, https://doi.org/10.1029/2010JD014265.

Potvin, C. K., and M. L. Flora, 2015: Sensitivity of Idealized Supercell Simulations to Horizontal Grid Spacing: Implications for Warn-on-Forecast. *Mon. Wea. Rev.*, **143**, 2998–3024, https://doi.org/10.1175/MWR-D-14-00416.1.

Prein, A. F., and Coauthors, 2015: A review on regional convection-permitting climate modeling: Demonstrations, prospects, and challenges. *Rev. Geophys.*, **53**, 323–361, https://doi.org/10.1002/2014RG000475.

Roberts, B., M. Xue, A. D. Schenkman, and D. T. Dawson, 2016: The role of surface drag in tornadogenesis within an idealized supercell simulation. *J. Atmos. Sci.*, **73**, 3371–3395, https://doi.org/10.1175/JAS-D-15-0332.1.

Schwartz, C. S., and Coauthors, 2009: Next-Day Convection-Allowing WRF Model Guidance: A Second Look at 2-km versus 4-km Grid Spacing. *Mon. Wea. Rev.*, **137**, 3351–3372, https://doi.org/10.1175/2009MWR2924.1.

Shi, X., F. K. Chow, R. L. Street, and G. H. Bryan, 2018a: An Evaluation of LES Turbulence Models for Scalar Mixing in the Stratocumulus-Capped Boundary Layer. *J. Atmos. Sci.*, **75**, 1499–1507, https://doi.org/10.1175/JAS-D-17-0392.1.

——, H. L. Hagen, F. K. Chow, G. H. Bryan, and R. L. Street, 2018b: Large-Eddy Simulation of the Stratocumulus-Capped Boundary Layer with Explicit Filtering and Reconstruction Turbulence Modeling. *J. Atmos. Sci.*, **75**, 611–637, https://doi.org/10.1175/JAS-D-17-0162.1.

——, F. K. Chow, R. L. Street, and G. H. Bryan, 2019: Key Elements of Turbulence Closures for Simulating Deep Convection at Kilometer-Scale Resolution. *Journal of Advances in Modeling Earth Systems*, **11**, 818–838, https://doi.org/10.1029/2018MS001446.

Shin, H. H., and S.-Y. Hong, 2015: Representation of the Subgrid-Scale Turbulent Transport in Convective Boundary Layers at Gray-Zone Resolutions. *Mon. Wea. Rev.*, **143**, 250–271, https://doi.org/10.1175/MWR-D-14-00116.1.

Simon, J. S., B. Zhou, J. D. Mirocha, and F. K. Chow, 2019: Explicit Filtering and Reconstruction to Reduce Grid Dependence in Convective Boundary Layer Simulations Using WRF-LES. *Mon. Wea. Rev.*, **147**, 1805–1821, https://doi.org/10.1175/MWR-D-18-0205.1.

Skamarock, W. C., 2004: Evaluating mesoscale nwp models using kinetic energy spectra. *Mon. Wea. Rev.*, **132**, 3019–3032, https://doi.org/10.1175/MWR2830.1.

——, and J. B. Klemp, 2008: A time-split nonhydrostatic atmospheric model for weather research and forecasting applications. *Journal of Computational Physics*, **227**, 3465–3485, https://doi.org/10.1016/j.jcp.2007.01.037.

Smagorinsky, J., 1963: General circulation experiments with the primitive equations. *Mon. Wea. Rev.*, **91**, 99–164, https://doi.org/10.1175/1520-0493(1963)091<0099:GCEWTP>2.3.CO;2.

Stolz, S., N. A. Adams, and L. Kleiser, 2001: The approximate deconvolution model for large-eddy simulations of compressible flows and its application to shock-turbulent-boundary-layer interaction. *Phys. Fluids*, **13**, 2985–3001, https://doi.org/10.1063/1.1397277.

Strauss, C., D. Ricard, C. Lac, and A. Verrelle, 2019: Evaluation of turbulence parametrizations in convective clouds and their environment based on a large-eddy simulation. *Quart. J. Roy. Meteor. Soc.*, **145**, 3195–3217, https://doi.org/10.1002/qj.3614.

Sullivan, P. P., T. W. Horst, D. H. Lenschow, C.-H. Moeng, and J. C. Weil, 2003: Structure of subfilter-scale fluxes in the atmospheric surface layer with application to large-eddy simulation modelling. *J. Fluid Mech.*, **482**, 101–139, https://doi.org/10.1017/S0022112003004099.

Takemi, T., and R. Rotunno, 2003: The Effects of Subgrid Model Mixing and Numerical Filtering in Simulations of Mesoscale Cloud Systems. *Mon. Wea. Rev.*, **131**, 2085–2101, https://doi.org/10.1175/1520-0493(2003)131<2085:TEOSMM>2.0.CO;2.

Tang, S. L., and D. J. Kirshbaum, 2020: On the sensitivity of deep- convection initiation to horizontal grid resolution. *Quart. J. Roy. Meteor. Soc.*, **146**, 1085–1105, https://doi.org/10.1002/qj.3726.

Thompson, R. L., and R. Edwards, 2000: An Overview of Environmental Conditions and Forecast Implications of the 3 May 1999 Tornado Outbreak. *Wea. Forecasting*, **15**, 682–699, https://doi.org/10.1175/1520-0434(2000)015<0682:AOOECA>2.0.CO;2.

Verrelle, A., D. Ricard, and C. Lac, 2015: Sensitivity of high-resolution idealized simulations of thunderstorms to horizontal resolution and turbulence parametrization. *Quart. J. Roy. Meteor. Soc.*, **141**, 433–448, https://doi.org/10.1002/qj.2363.

Verrelle, A., D. Ricard, and C. Lac, 2017: Evaluation and Improvement of Turbulence Parameterization inside Deep Convective Clouds at Kilometer-Scale Resolution. *Mon. Wea. Rev.*, **145**, 3947–3967, https://doi.org/10.1175/MWR-D-16-0404.1.

Vreman, B., B. Geurts, and H. Kuerten, 1996: Large-eddy simulation of the temporal mixing layer using the Clark model. *Theor. Comput. Fluid Dyn.*, **8**, 309–324, https://doi.org/10.1007/BF00639698.

Weisman, M. L., W. C. Skamarock, and J. B. Klemp, 1997: The resolution dependence of explicitly modeled convective systems. *Mon. Wea. Rev.*, **125**, 527–548, https://doi.org/10.1175/1520-0493(1997)125<0527:TRDOEM>2.0.CO;2.

Wyngaard, J. C., 2004: Toward Numerical Modeling in the “Terra Incognita.” *J. Atmos. Sci.*, **61**, 1816–1826, https://doi.org/10.1175/1520-0469(2004)061<1816:TNMITT>2.0.CO;2.

Xue, M., K. K. Droegemeier, and V. Wong, 2000: The Advanced Regional Prediction System (ARPS)–A multi-scale nonhydrostatic atmospheric simulation and prediction model. Part I: Model dynamics and verification. *Meteor. Atmos. Phys.*, **75**, 161–193, https://doi.org/10.1007/s007030070003.

——, and Coauthors, 2001: The Advanced Regional Prediction System (ARPS)–A multi-scale nonhydrostatic atmospheric simulation and prediction tool. Part II: Model physics and applications. *Meteor. Atmos. Phys.*, **76**, 143–165, https://doi.org/10.1007/s007030170027.

——, D. Wang, J. Gao, K. Brewster, and K. K. Droegemeier, 2003: The Advanced Regional Prediction System (ARPS), storm-scale numerical weather prediction and data assimilation. *Meteor. Atmos. Phys.*, **82**, 139–170, https://doi.org/10.1007/s00703-001-0595-6.

Zhang, X., J.-W. Bao, B. Chen, and E. D. Grell, 2018: A Three-Dimensional Scale-Adaptive Turbulent Kinetic Energy Scheme in the WRF-ARW Model. *Mon. Wea. Rev.*, **146**, 2023–2045, https://doi.org/10.1175/MWR-D-17-0356.1.

Zhou, B., and F. K. Chow, 2011: Large-eddy simulation of the stable boundary layer with explicit filtering and reconstruction turbulence modeling. *J. Atmos. Sci.*, **68**, 2142–2155, https://doi.org/10.1175/2011JAS3693.1.

Zhu, K., and Coauthors, 2018: Evaluation of Real-Time Convection-Permitting Precipitation Forecasts in China During the 2013-2014 Summer Season. *J. Geophys. Res.*, **123**, 1037–1064, https://doi.org/10.1002/2017JD027445.

List of Figures

FIG. 1. Horizontally-averaged profiles of (a) potential temperature θ, (b) water vapor mixing ratio q_v, (c) nonprecipitating water content q_{np} (the sum of cloud water and cloud ice mixing ratios) and (d) precipitating water content q_p (the sum of rain water, snow and hail mixing ratios) (dashed line) along with their respective vertical SGS fluxes for different horizontal resolutions (color solid lines) and the resolved vertical fluxes from LES (black lines) at 1800 s. Vertical profiles of the SGS-to-total flux ratios for (e) θ, (f) q_v, (g) q_{np} and (h) q_p. Zero values are represented by dotted lines. Angle brackets represent horizontal averaging. In (a-d), mean variables are plotted with dashed lines (top axes) and their SGS fluxes with solid lines (bottom axes), the heights where $\langle \overline{w''c''}^{\Delta} \times (\partial \bar{c}^{\Delta}/\partial z)\rangle > 0$ for Δ = 1 km are shaded.

FIG. 2. Horizontal cross sections of the filtered (a) $\overline{u''\theta''}^{\Delta}$, (b) $\overline{u''\theta''}^{\Delta} \times (\partial\bar{\theta}^{\Delta}/\partial x)$, (c) $\overline{v''\theta''}^{\Delta}$, (d) $\overline{v''\theta''}^{\Delta} \times (\partial\bar{\theta}^{\Delta}/\partial y)$, (e) $\overline{w''\theta''}^{\Delta}$, and (f) $\overline{w''\theta''}^{\Delta} \times (\partial\bar{\theta}^{\Delta}/\partial z)$ from LES at 8 km AGL with Δ = 1 km. Thin solid contours represent the cloud boundary where $q_{np} = 1.0\times10^{-6}$ kg kg^{-1}. Dashed contours outline the updraft core where w $\geq$ 10 m s^{-1}. Thick solid lines AB and CD indicate the locations of the vertical cross sections presented in FIG. 3.

FIG. 3. As FIG. 2, but for the vertical cross sections along the horizontal solid lines AB (for a, b, e, and f) and CD (for c and d) in FIG. 2. Arrows represent storm-related (u, w) (for a, b, e, and f) and (v, w) (for c and d) wind vectors.

FIG. 4. Profiles of the correlation coefficients r between diagnosed and modeled SGS fluxes (a) $\overline{w''\theta''}^{\Delta}$, (b) $\overline{w''q_v''}^{\Delta}$, (c) $\overline{w''q_{np}''}^{\Delta}$, (d) $\overline{w''q_p''}^{\Delta}$, (e) $\overline{u''\theta''}^{\Delta}$, (f) $\overline{u''w''}^{\Delta}$, (g) $\overline{u''u''}^{\Delta}$ and (h)

$\overline{w''w''}^{\Delta}$ at different horizontal resolutions from 25 to 40 min. Solid and dashed lines represent correlation of modeled fluxes with the Hgrad and the TKE closures respectively.

FIG. 5. Scheme coefficients in the Hgrad closure for (a) vertical $C_{s,v}$, (b) horizontal $C_{s,h}$, and (c) momentum C_m as functions of the horizontal resolution Δ. Circles represent the depth-averaged temporal mean between 1 and 14 km AGL from 25 to 40 min, and the error bars indicate one standard deviation from the mean. The dashed lines represent empirical power-law fits.

FIG. 6. Horizontal-averaged profiles of $\overline{w''\theta''}^{\Delta}$ (top row) and $\overline{u''\theta''}^{\Delta}$ (bottom row) at horizontal resolutions of (a, f) 250 m, (b, g) 500 m, (c, h) 1 km, (d, i) 2 km, and (e, j) 4 km. Legends with suffix "D" represent the *a priori* diagnosed fluxes, those with suffix "R" represent fluxes from *a posteriori* online simulations. Note the different x-axis values.

FIG. 7. Horizontal cross sections for modeled SGS fluxes of $\overline{u''\theta''}^{\Delta}$ (top row), $\overline{v''\theta''}^{\Delta}$ (middle row), and $\overline{w''\theta''}^{\Delta}$ (bottom row) at 8 km AGL with Δ = 1 km. The left and right columns represent results from the TKE and the Hgrad closures, respectively.

FIG. 8. As FIG. 7, but for the vertical cross sections along the horizontal solid lines in FIG. 2.

FIG. 9. Horizontally averaged profiles for TKE at horizontal resolutions of (a) 250 m, (b) 500 m, (c) 1 km, (d) 2 km, and (e) 4 km.

FIG. 10. Vertical profiles of the horizontally-averaged resolved heat flux $\overline{w''\theta''}^{\mathrm{L}} - \overline{w''\theta''}^{\Delta}$(dashed lines) and total heat flux $\overline{w''\theta''}^{\mathrm{L}}$ (solid lines) at horizontal resolutions of (a) 250 m, (b) 500 m, (c) 1 km, (d) 2 km, and (e) 4 km. Results are from the *a posteriori* online simulations.

FIG. 11. As FIG. 7, but for the *a posteriori* online simulations.

FIG. 12. As FIG. 8, but for the *a posteriori* online simulations.

FIG. 13. Horizontal (left column) and vertical (right column) cross sections of wind vectors and simulated reflectivity field (color shaded) for (a, b) filtered LES, (c, d) simulation with TKE scheme, and (e, f) simulation with Hgrad scheme. The horizontal cross sections are at 1 km AGL, and the vertical cross sections are through the updraft cores, their locations are indicated by the thick solid lines in a, c and e. Vertical velocity (thin contours at 1 m s^{-1} intervals begin from 5 m s^{-1}) and the outline of cold pool gust front (blue line, the −0.5 K perturbation θ from base state at 10 m AGL) are also presented at the left column. The horizontal grid spacing for TKE and Hgrad simulations is 1 km and the plotted fields are at 2100 s.

FIG. 14. Time series of domain-averaged precipitation rate.

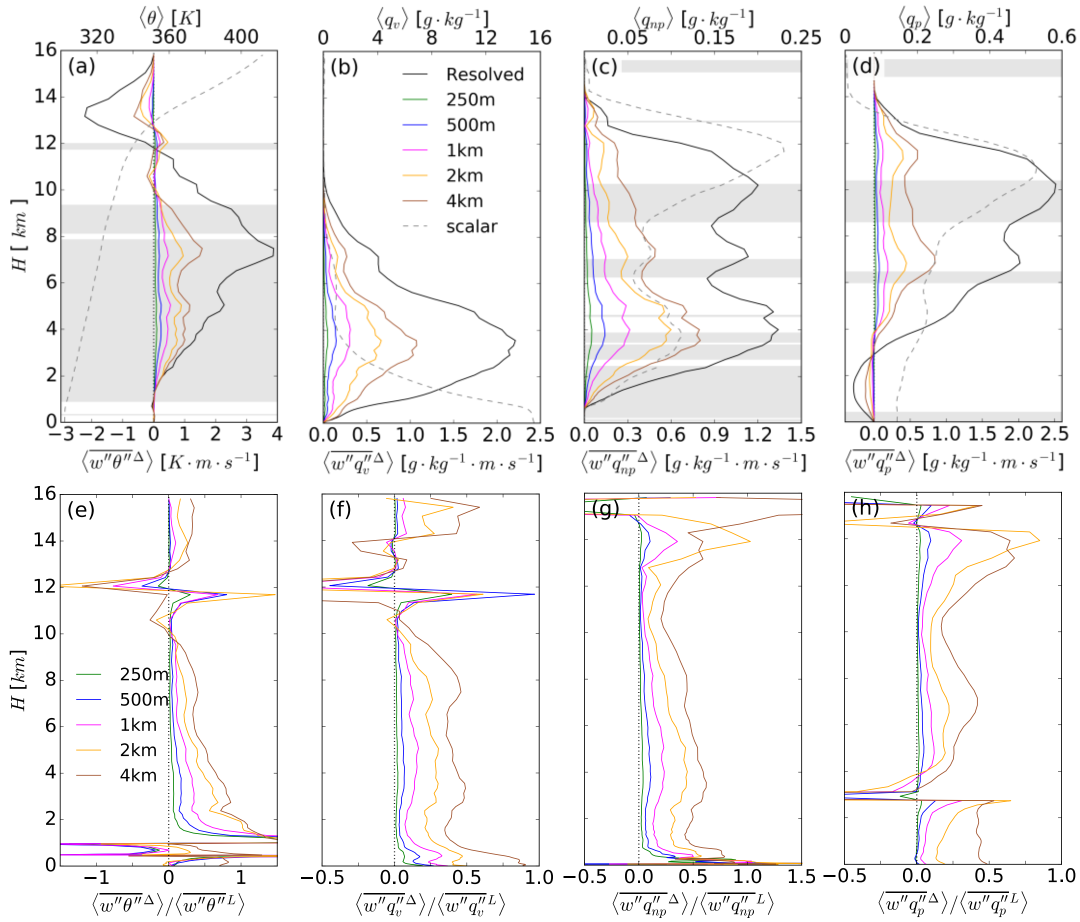

FIG. 1. Horizontally-averaged profiles of (a) potential temperature θ, (b) water vapor mixing ratio q_v, (c) nonprecipitating water content q_{np} (the sum of cloud water and cloud ice mixing ratios) and (d) precipitating water content q_p (the sum of rain water, snow and hail mixing ratios) (dashed line) along with their respective vertical SGS fluxes for different horizontal resolutions (color solid lines) and the resolved vertical fluxes from LES (black lines) at 1800 s. Vertical profiles of the SGS-to-total flux ratios for (e) θ, (f) q_v, (g) q_{np} and (h) q_p. Zero values are represented by dotted lines. Angle brackets represent horizontal averaging. In (a-d), mean variables are plotted with dashed lines (top axes) and their SGS fluxes with solid lines (bottom axes), the heights where $\langle \overline{w''c''}^{\Delta} \times (\partial \bar{c}^{\Delta}/\partial z)\rangle > 0$ for Δ = 1 km are shaded.

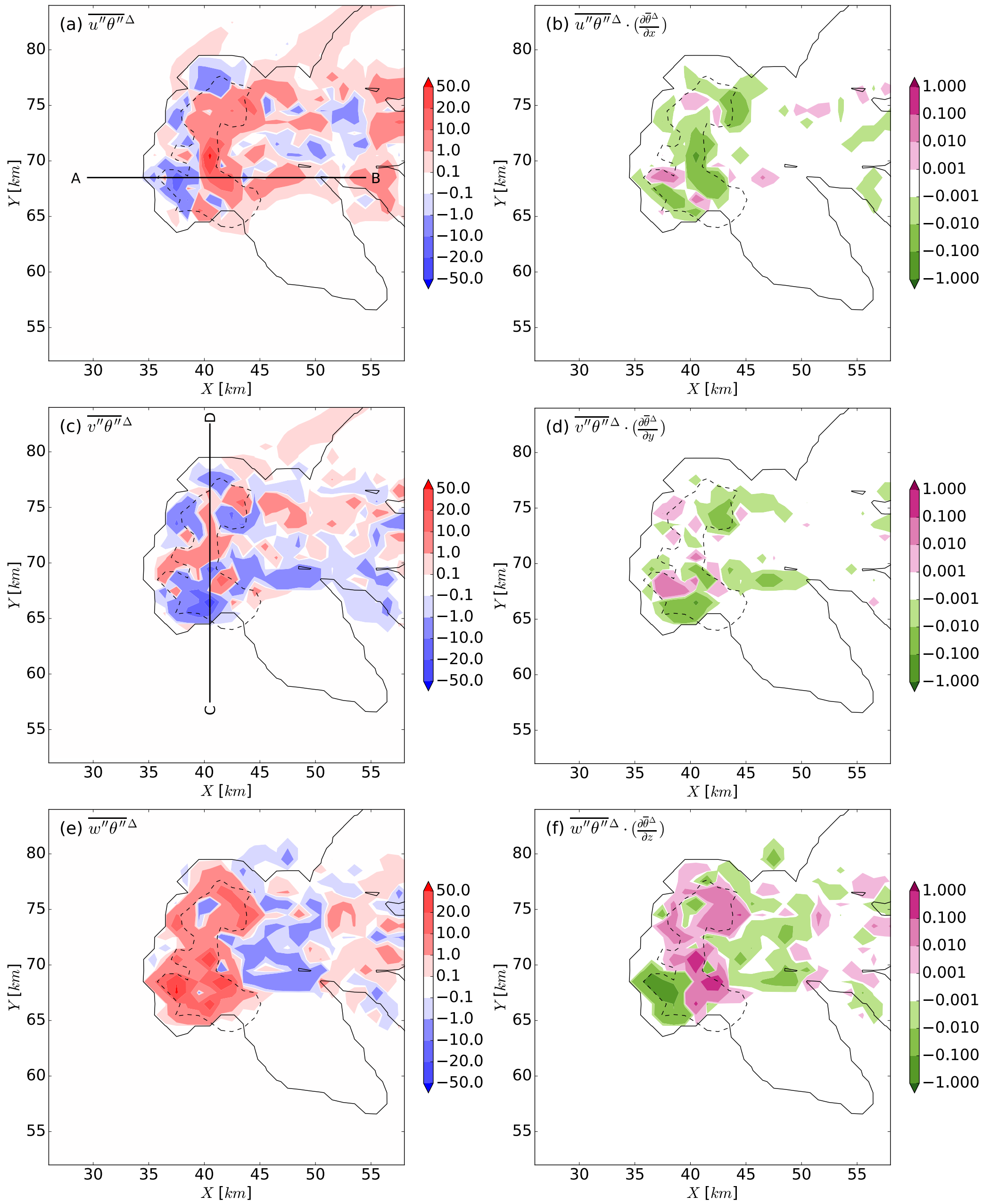

FIG. 2. Horizontal cross sections of the filtered (a) $\overline{u''\theta''}^{\Delta}$, (b) $\overline{u''\theta''}^{\Delta} \times (\partial\bar{\theta}^{\Delta}/\partial x)$, (c) $\overline{v''\theta''}^{\Delta}$, (d) $\overline{v''\theta''}^{\Delta} \times (\partial\bar{\theta}^{\Delta}/\partial y)$, (e) $\overline{w''\theta''}^{\Delta}$, and (f) $\overline{w''\theta''}^{\Delta} \times (\partial\bar{\theta}^{\Delta}/\partial z)$ from LES at 8 km AGL with Δ = 1 km. Thin solid contours represent the cloud boundary where $q_{np} = 1.0\times10^{-6}$ kg kg^{-1}. Dashed contours outline the updraft core where $w \geq 10$ m s^{-1}. Thick solid lines AB and CD indicate the locations of the vertical cross sections presented in FIG. 3.

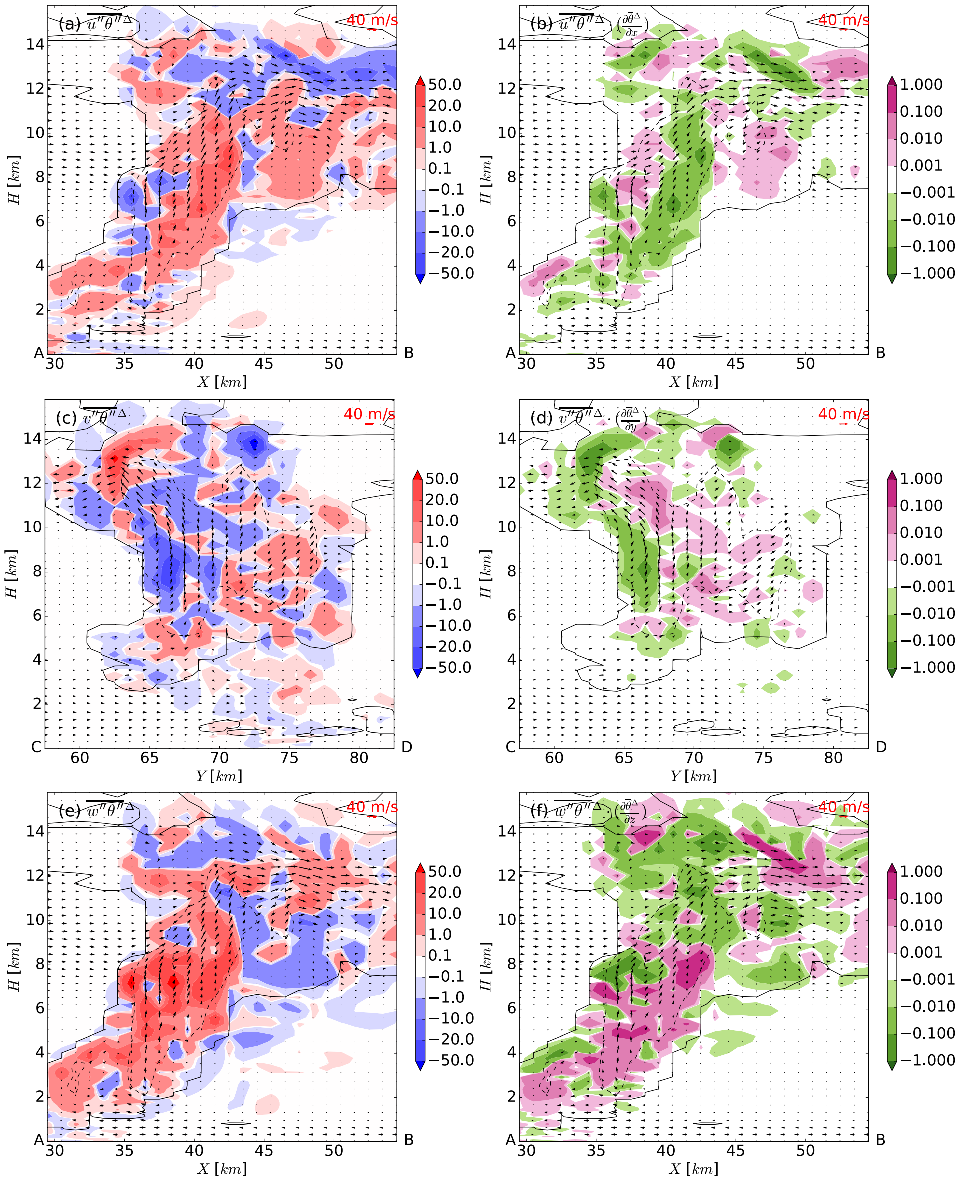

FIG. 3. As FIG. 2, but for the vertical cross sections along the horizontal solid lines AB (for a, b, e, and f) and CD (for c and d) in FIG. 2. Arrows represent storm-related (u, w) (for a, b, e, and f) and (v, w) (for c and d) wind vectors.

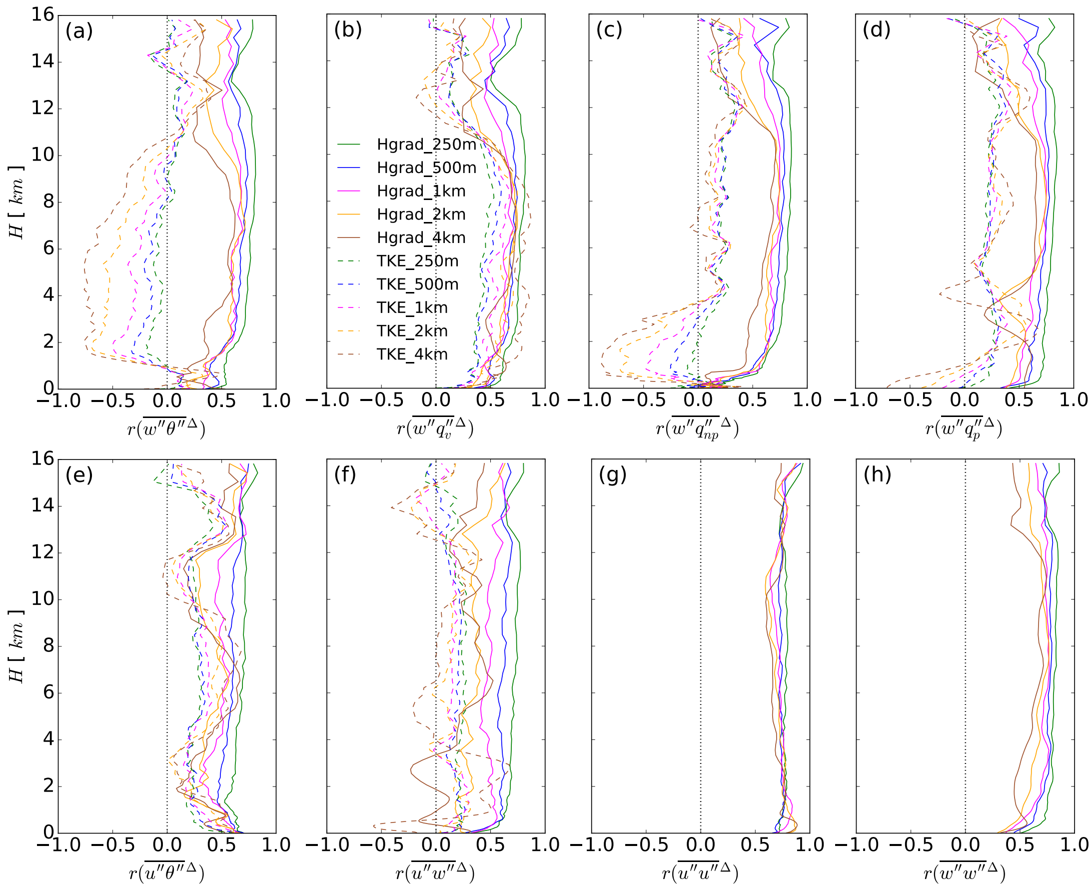

FIG. 4. Profiles of the correlation coefficients r between diagnosed and modeled SGS fluxes (a) $\overline{w''\theta''}^{\Delta}$, (b) $\overline{w''q_v''}^{\Delta}$, (c) $\overline{w''q_{np}''}^{\Delta}$, (d) $\overline{w''q_p''}^{\Delta}$, (e) $\overline{u''\theta''}^{\Delta}$, (f) $\overline{u''w''}^{\Delta}$, (g) $\overline{u''u''}^{\Delta}$ and (h) $\overline{w''w''}^{\Delta}$ at different horizontal resolutions from 25 to 40 min. Solid and dashed lines represent correlation of modeled fluxes with the Hgrad and the TKE closures respectively.

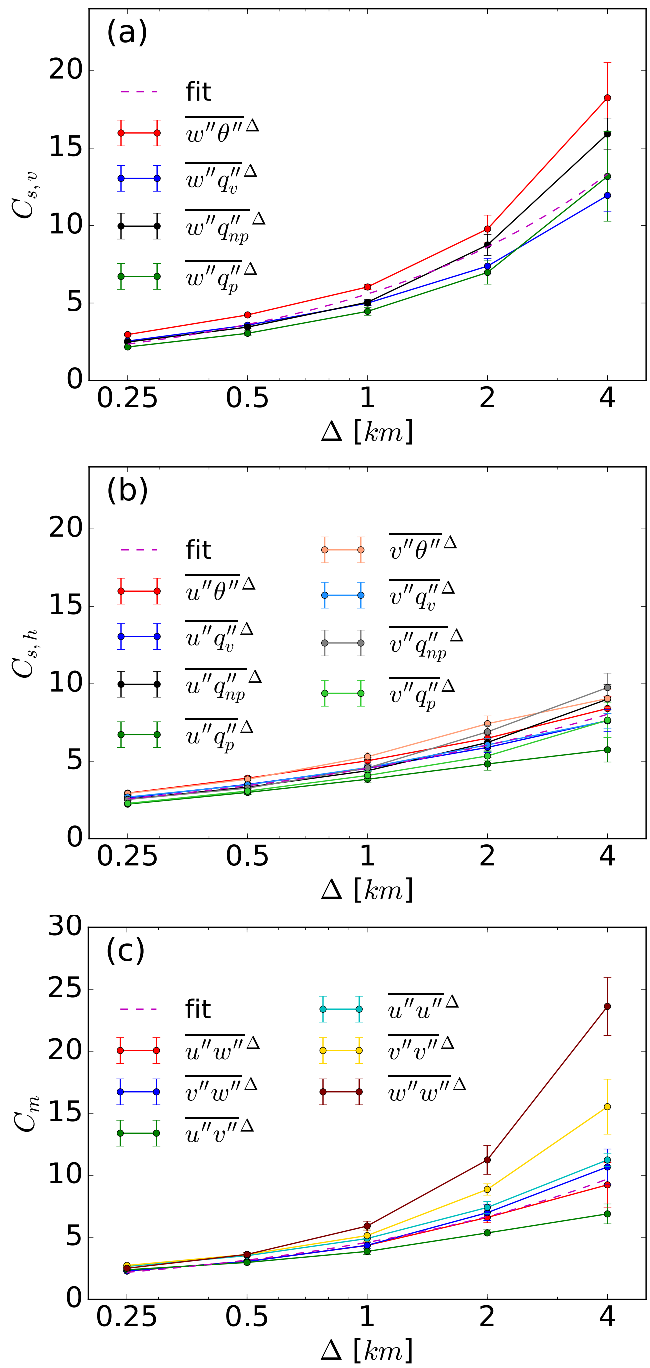

FIG. 5. Scheme coefficients in the Hgrad closure for (a) vertical $C_{s,v}$, (b) horizontal $C_{s,h}$, and (c) momentum C_m as functions of the horizontal resolution Δ. Circles represent the depth-averaged temporal mean between 1 and 14 km AGL from 25 to 40 min, and the error bars indicate one standard deviation from the mean. The dashed lines represent empirical power-law fits.

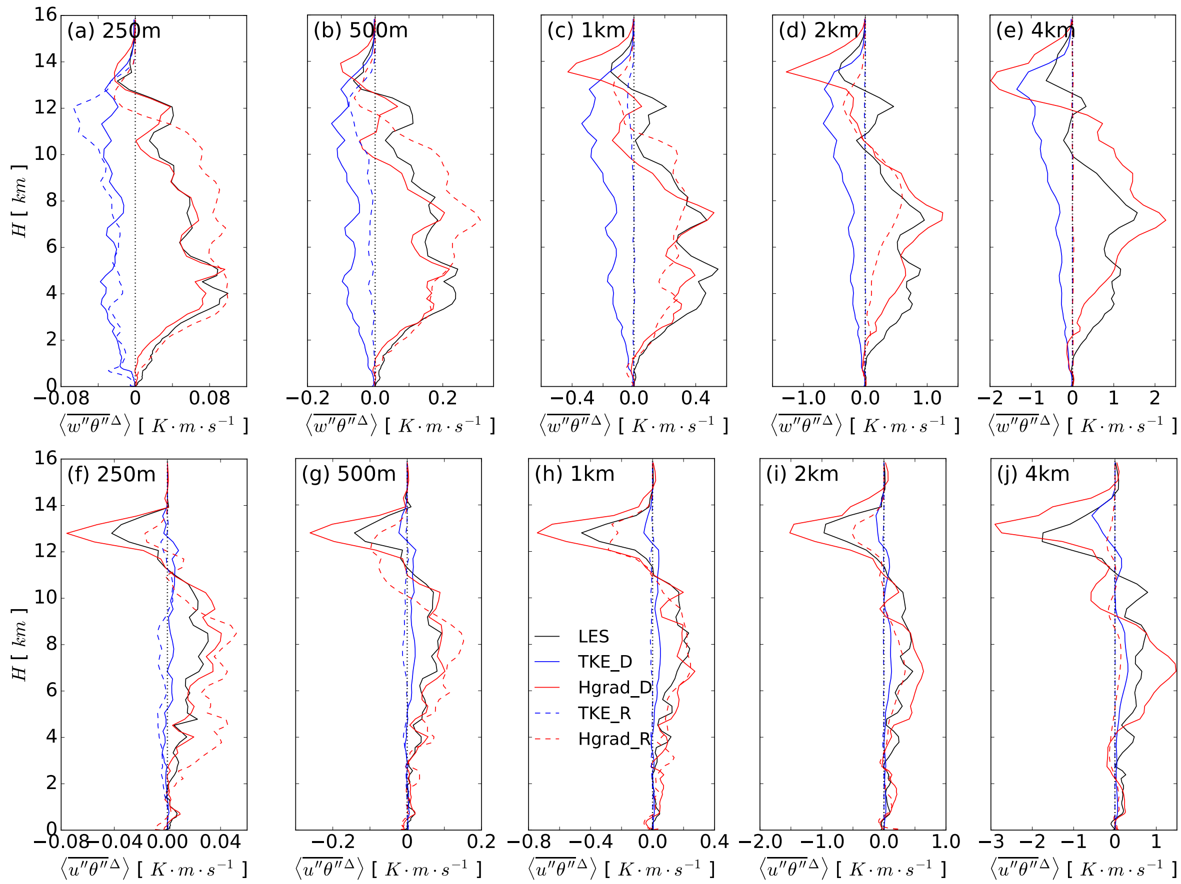

FIG. 6. Horizontal-averaged profiles of $\overline{w''\theta''}^{\Delta}$ (top row) and $\overline{u''\theta''}^{\Delta}$ (bottom row) at horizontal resolutions of (a, f) 250 m, (b, g) 500 m, (c, h) 1 km, (d, i) 2 km, and (e, j) 4 km. Legends with suffix "D" represent the *a priori* diagnosed fluxes, those with suffix "R" represent fluxes from *a posteriori* online simulations. Note the different x-axis values.

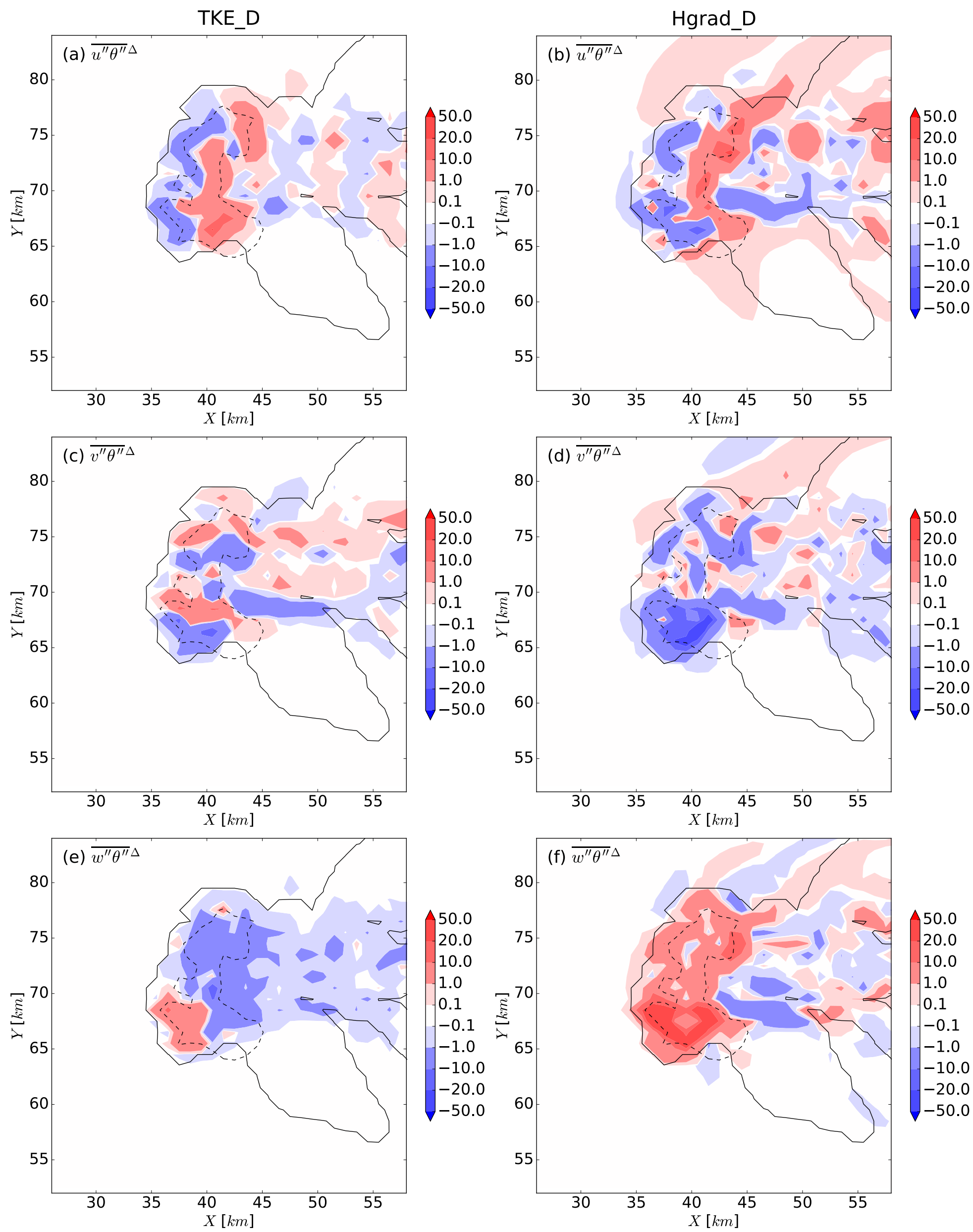

FIG. 7. Horizontal cross sections for modeled SGS fluxes of $\overline{u''\theta''}^{\Delta}$ (top row), $\overline{v''\theta''}^{\Delta}$ (middle row), and $\overline{w''\theta''}^{\Delta}$ (bottom row) at 8 km AGL with Δ = 1 km. The left and right columns represent results from the TKE and the Hgrad closures, respectively.

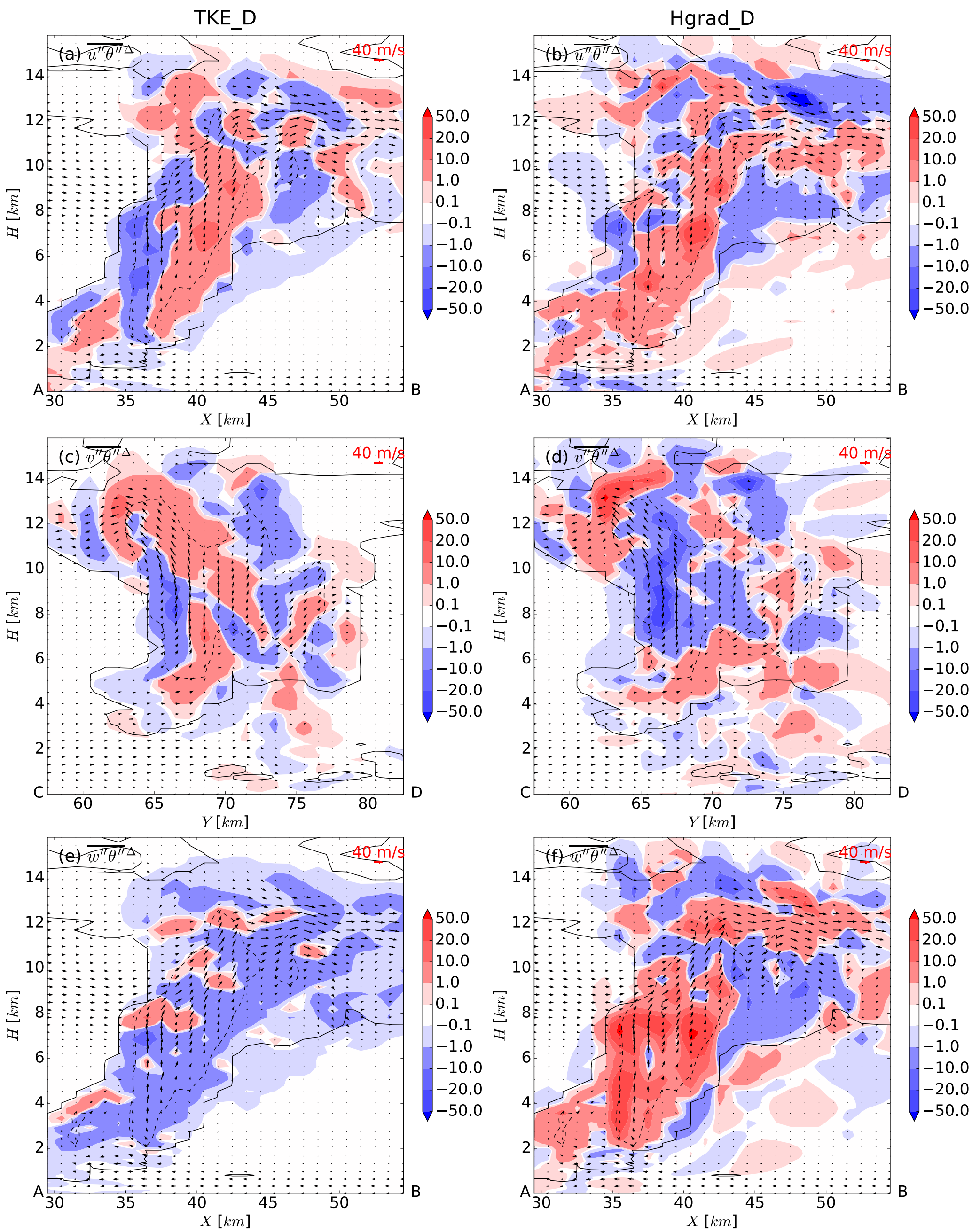

FIG. 8. As FIG. 7, but for the vertical cross sections along the horizontal solid lines in FIG. 2.

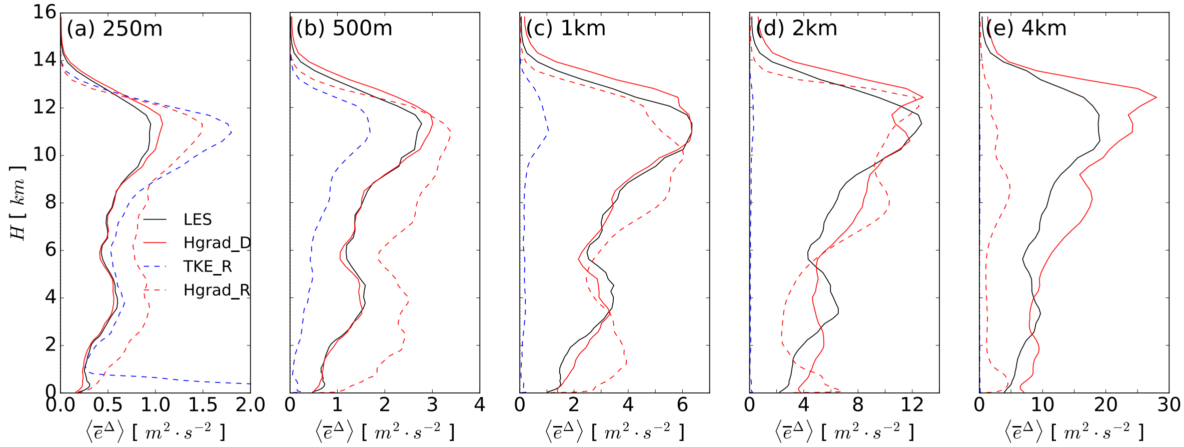

FIG. 9. Horizontally averaged profiles for TKE at horizontal resolutions of (a) 250 m, (b) 500 m, (c) 1 km, (d) 2 km, and (e) 4 km.

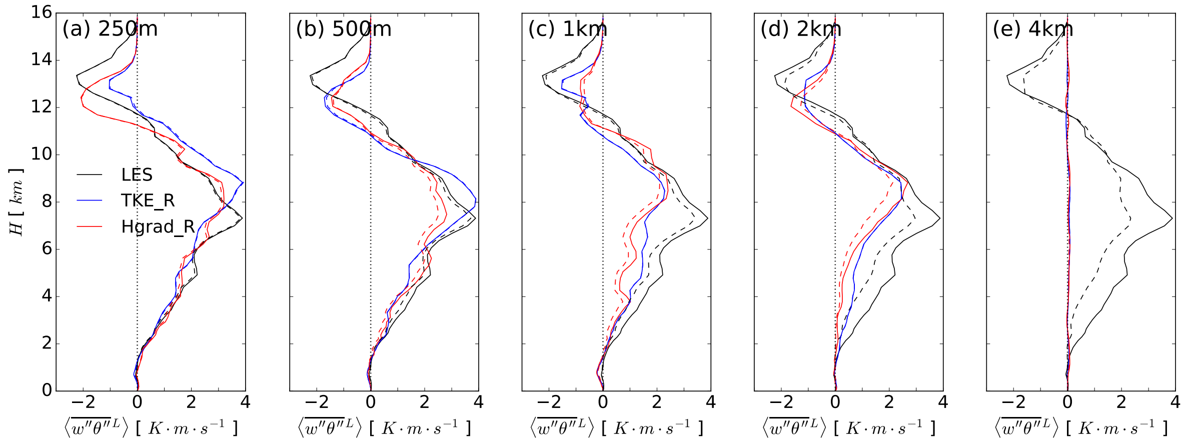

FIG. 10. Vertical profiles of the horizontally-averaged resolved heat flux $\overline{w''\theta''}^{L} - \overline{w''\theta''}^{\Delta}$ (dashed lines) and total heat flux $\overline{w''\theta''}^{L}$ (solid lines) at horizontal resolutions of (a) 250 m, (b) 500 m, (c) 1 km, (d) 2 km, and (e) 4 km. Results are from the *a posteriori* online simulations.

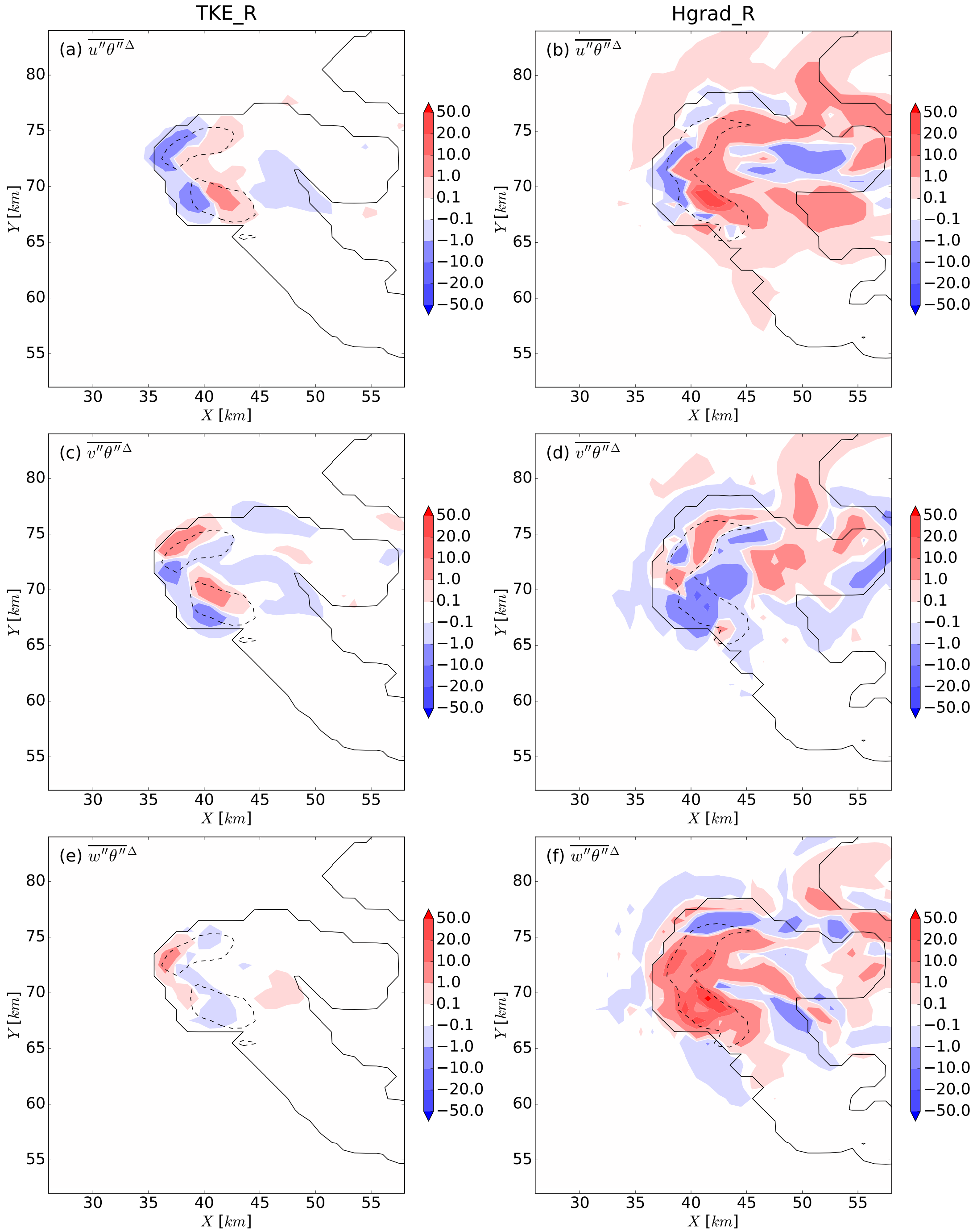

FIG. 11. As FIG. 7, but for the *a posteriori* online simulations.

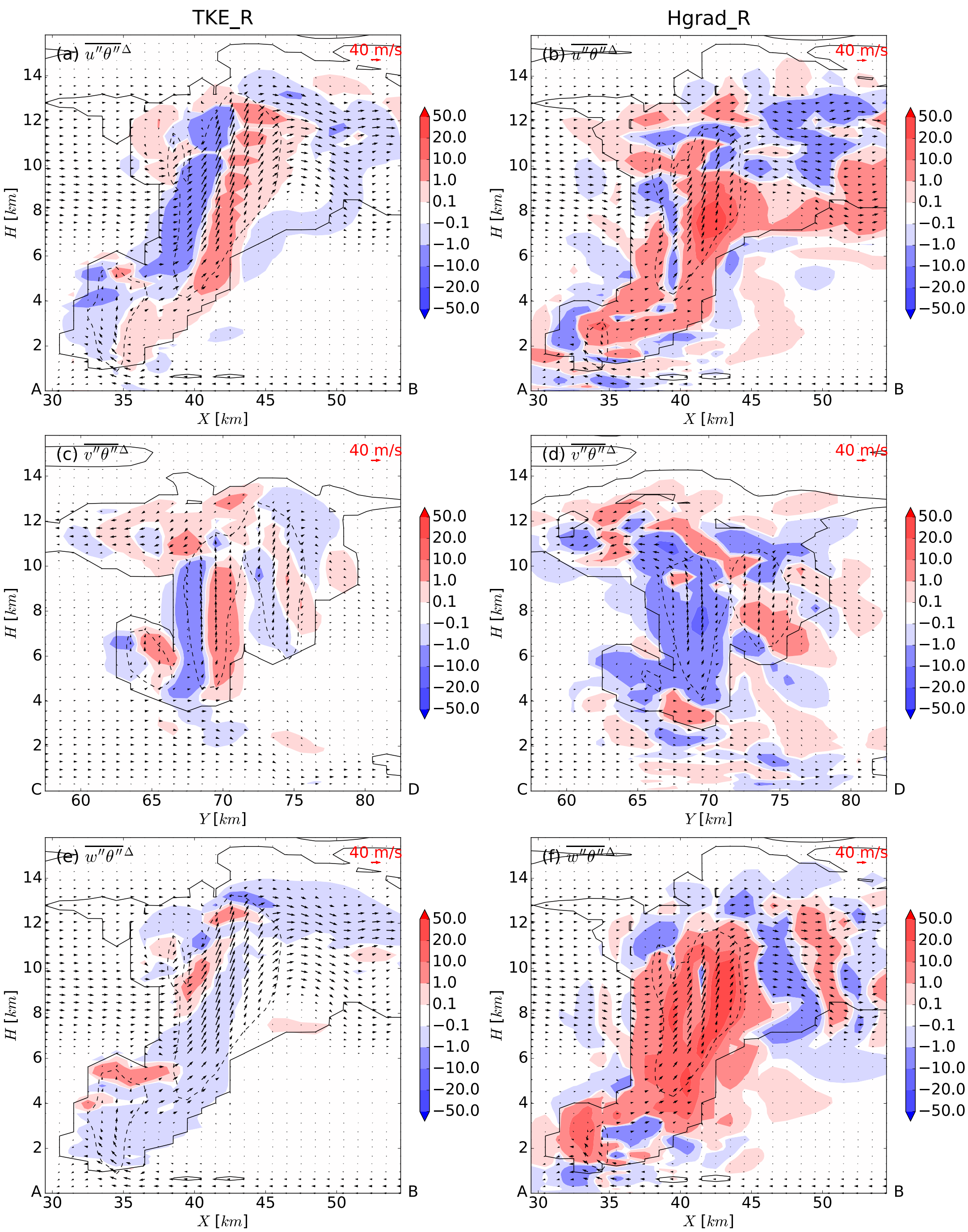

FIG. 12. As FIG. 8, but for the *a posteriori* online simulations.

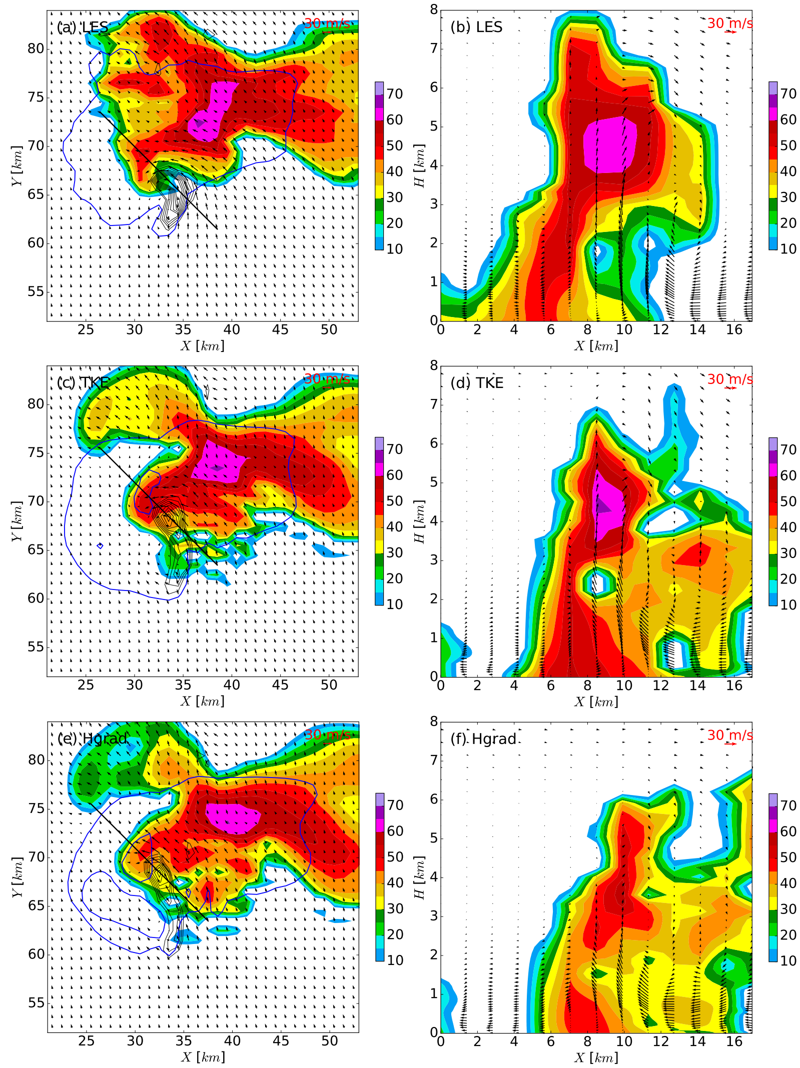

FIG. 13. Horizontal (left column) and vertical (right column) cross sections of wind vectors and simulated reflectivity field (color shaded) for (a, b) filtered LES, (c, d) simulation with TKE scheme, and (e, f) simulation with Hgrad scheme. The horizontal cross sections are at 1 km AGL, and the vertical cross sections are through the updraft cores, their locations are indicated by the thick solid lines in a, c and e. Vertical velocity (thin contours at 1 m s^{-1} intervals begin from 5 m s^{-1}) and the outline of cold pool gust front (blue line, the –0.5 K perturbation θ from base state at 10 m AGL) are also presented at the left column. The horizontal grid spacing for TKE and Hgrad simulations is 1 km and the plotted fields are at 2100 s.

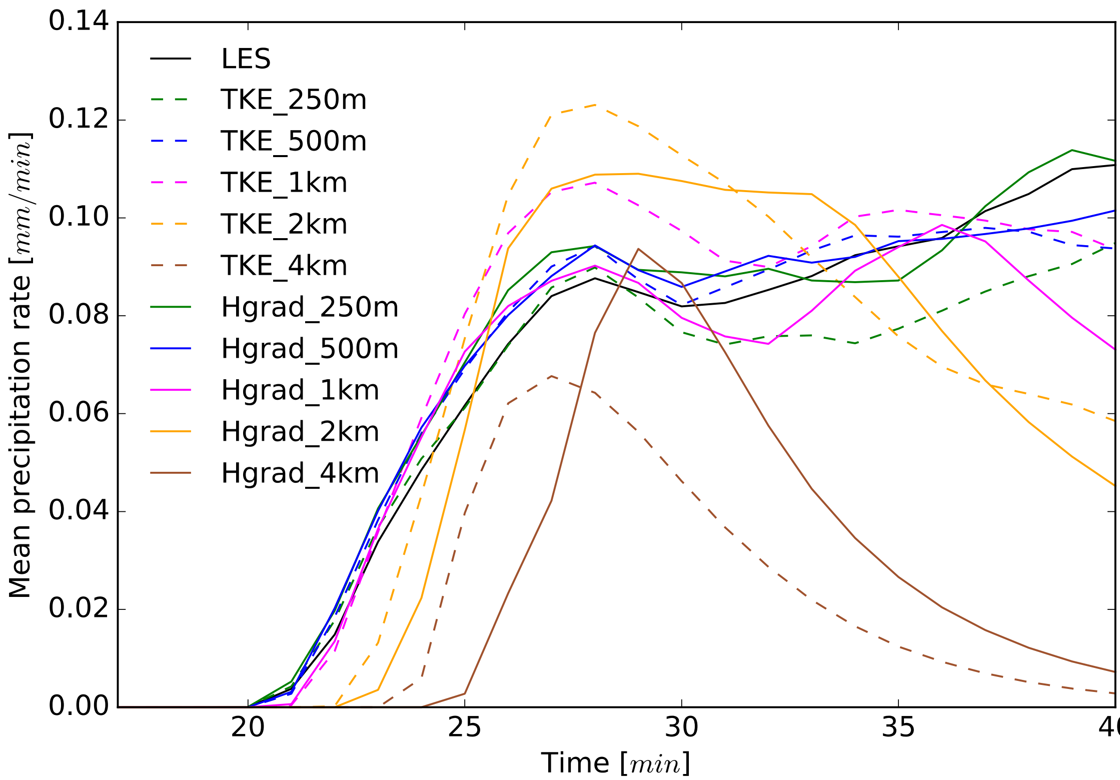

FIG. 14. Time series of domain-averaged precipitation rate.

Non-Rendered Figure 14

Click here to access/download
Non-Rendered Figure
fig14.Rainfall_1min.pdf